J. Fluid Mech. (2018), *vol.* 853, *pp.* 301–332.
doi:10.1017/jfm.2018.573

Vibrations of a square cylinder submerged in a wake

Rajesh Bhatt[1,2] **and Md. Mahbub Alam**[1,2,†]

[1]Institute for Turbulence-Noise-Vibration Interactions and Control, Shenzhen Graduate School, Harbin Institute of Technology, 518055 Shenzhen, PR China

[2]Digital Engineering Laboratory of Offshore Equipment, Harbin Institute of Technology, 518055 Shenzhen, PR China

(Received 25 January 2018; revised 10 May 2018; accepted 16 July 2018; first published online 23 August 2018)

A numerical investigation is conducted on the flow around and vibration response of an elastic square cylinder (side width D) in the wake of a stationary cylinder at Reynolds numbers of $Re = 100$ and 200 based on D and the free-stream velocity. The downstream cylinder, referred to as the wake cylinder, is allowed to vibrate in the transverse direction only. The reduced velocity U_r is varied from 1 to 30. Cylinder centre-to-centre spacing ratios of $L^*(=L/D) = 2$ and 6 are considered. Simulations are also conducted for a single isolated cylinder, and the results are compared with those for the wake cylinder. The focus is given to vibration response, frequency response, fluctuating lift force, phase relationship between the lift and displacement, work done and the flow structure modification during the cylinder vibration. The results reveal that the dependence of the Strouhal number St on U_r can distinguish different branches more appropriately than that of the vibration amplitude on U_r. The vibration response of the single cylinder at $Re = 100$ is characterized by the initial, lower and desynchronization branches. On the other hand, that at $Re = 200$ undergoes initial, lower and galloping branches. The galloping involves the characteristics of both the initial and the lower branches or the initial and the desynchronization branches depending on U_r. For the wake cylinder, the gap flow has a significant impact on the vibration response, leading to (i) the absence of galloping at either Re and L^*, (ii) the presence of an upper branch at $Re = 200$, $L^* = 6$ and (iii) an initial branch of different characteristics at $Re = 100$, $L^* = 6$. The different facets are discussed in terms of wake structures, work done and phase lag between lift and displacement.

Key words: flow–structure interactions, vortex shedding, wakes

1. Introduction

Square-sectioned structures are common in many engineering applications such as bridges, offshore platforms, high-rise buildings, and so on. The study of flow-induced vibrations (FIV) of these structures has great importance, especially in assessing the stability of the structures. Alternating vortex shedding and associated fluid–structure interactions generate periodic fluctuating forces on the surfaces of structures, resulting

† Email addresses for correspondence: alam@hit.edu.cn, alamm28@yahoo.com

in self-excited vibrations. Vortex-induced vibration (VIV) and galloping are the most common self-excited vibration phenomena. Vortex-induced vibration occurs when the shedding frequency locks in to the structural natural frequency, while galloping vibration, in general, takes place with the shedding frequency higher or lower (Nakamura & Matsukawa 1987; Nakamura & Hirata 1991) than the structural natural frequency. Flow-induced vibrations have attracted widespread attention in the past decades, involving many independent parameters, e.g. mass ratio m^*, damping ratio ζ, natural frequency f_n, Reynolds number Re, reduced velocity U_r, structure shape, turbulent intensity, etc. In most previous studies on flow-induced vibrations of cylinders, U_r is treated as an independent parameter (Singh & Mittal 2005; Zhao, Cheng & Zhou 2013), while in some other studies, U_r is regarded as a function of Re (Singh & Biswas 2013; Sen & Mittal 2015). The Reynolds number involves the flow velocity, fluid properties and structure dimension. On the other hand, U_r integrates the flow velocity, structure dimension and structure elasticity. The Reynolds number and U_r are, therefore, functions of each other. As such, given the same U_r ranges, the vibration response characteristics may be different in different Re ranges (e.g. Barrero-Gil, Sanz-Andres & Roura 2009; Kumar, Sing & Sen 2018).

In order to understand the relationship between the flow structure, structural vibration amplitude and vibration frequency, forced vibration tests of a cylinder (square/rectangular) were conducted by, e.g., Nakamura & Mizota (1975), Bearman & Obasaju (1982) and Singh *et al.* (2009). Nakamura & Mizota (1975) experimentally examined the lift and wake of a square cylinder given forced vibration in the transverse direction. When the vibration frequency coincides with the shedding frequency, the phase lag between the lift and the wake velocity shows an abrupt change, which was identified to be a key point for solving VIV problems. Singh *et al.* (2009) studied the forced vibrations of a square cylinder for an excitation-to-natural shedding frequency ratio f_e/f_v of 0.5–3.0 at a constant amplitude ratio A^* $(= A/D)$ of 0.2 at $Re = 100$ and 150, where D is the cylinder width. Lock-in occurred for $f_e/f_v = 0.95$–1.2 and 0.8–1.3 at $Re = 100$ and 150 respectively, where the f_v was modified and synchronized with the f_e.

Free vibrations of a two-dimensional square cylinder with one and two degrees of freedom were experimentally and numerically conducted by Su *et al.* (2007), Sen & Mittal (2011, 2015), He, Zhou & Bao (2012), Singh & Biswas (2013), Cui *et al.* (2015) and Zhao (2015). To understand the VIV mechanism of a square cylinder at subcritical Re, Singh & Biswas (2013) varied m^*, Re and the reduced velocity U_r $(= U/f_nD$, where U is the free-stream velocity). They reported that the phase lag ϕ between the lift force and the transverse displacement depends on Re, m^* and U_r. Cui *et al.* (2015) investigated the flow-induced vibration of square and rectangular cylinders for incident angles of $\alpha = 0°$–$90°$. At $\alpha = 0°$, the response of the cylinder is dominated by galloping with $\phi \approx 0°$. Sen & Mittal (2015) studied the effect of m^* and Re (or U_r) on in-line and transverse free vibrations of a square cylinder. For a low mass ratio $m^* = 1$, the cylinder response is characterized by initial and lower branches; no galloping is observed. Galloping, however, occurs for $m^* \geqslant 5$. They identified three vortex shedding modes, i.e. 2S, C(2S) and (2P + 2S). Modes 2S and C(2S) are involved in VIV, whereas the galloping vibration features the 2S mode for $A^* < 0.7$ and the 2P + 2S mode for $A^* > 0.7$.

The literature has improved our understanding of the FIV of a single structure. Most structures on the land and in the ocean, however, appear in a group. The physics of the flow around a group of structures, involving complex mutual interactions between the structures, cannot be directly extrapolated from the knowledge on

a single structure. The flow around two structures, however, provides an excellent model to understand the mutual interactions between the structures in a group. As such, Sakamoto, Haniu & Obata (1987) examined the dependence on the centre-to-centre spacing ratio L^* ($= L/D = 1.5$–41) of the flow around two stationary square cylinders in tandem arrangements. They observed two major flow regimes depending on L^*, i.e. the reattachment flow regime ($L^* < 4$) and the coshedding flow regime ($L^* > 4$). In the former regime, the shear layers separating from the upstream cylinder reattach on the downstream cylinder, and vortex shedding occurs only from the downstream cylinder. On the other hand, in the latter regime, the shear layers roll up and form a vortex street in the gap between the cylinders, the two cylinders shedding vortices individually. Their shedding frequencies are identical at $4 < L^* < 28$ and different at $L^* > 28$, smaller for the downstream cylinder. The arrival of the upstream-cylinder-generated vortices triggers the vortex shedding from the downstream cylinder for the former L^* range and cannot for the latter L^* range. Sohankar (2012) performed two-dimensional and three-dimensional unsteady simulations to study the flow over two tandem stationary square cylinders with $L^* = 1.3$–13 at $Re = 130$, 150 and 500. Depending on L^*, three major flow regimes were distinguished: the single-body regime ($L^* < 1.5$), the reattachment regime ($L^* < 5$) and the coshedding regime ($L^* \geqslant 5$).

When an elastically mounted cylinder is placed in the wake of an upstream stationary cylinder, the flow around the former cylinder becomes more complex compared with its stationary counterpart. Mithun & Tiwari (2014) numerically examined the wake characteristics of two tandem square cylinders at $Re = 100$ that were given an inphase forced vibration at the same f_e and A^* ($= 0.4$). The vibrations of the cylinders drastically altered the wake from the corresponding stationary counterpart. When f_e was increased, ϕ jumped from 0° to 180° in the lock-in regime. More *et al.* (2015) experimentally investigated the flow around two square cylinders in tandem arrangements for $L^* = 1.5$–5. The upstream cylinder with $A^* = 0.1$ oscillated at higher harmonics of the vortex shedding frequency of a stationary cylinder when the downstream cylinder was kept fixed. They observed a strong effect of L^* on the vortex shedding process and flow structure. Jaiman, Pillalamarri & Guan (2016) examined, at $Re = 200$, the free vibration response of a downstream square cylinder at a fixed $L^* = 4$ and $m^* = 5$ when an upstream square cylinder was kept stationary. They identified initial and lower branches in the lock-in regime, and desynchronization and galloping branches beyond the lock-in regime. They found $\phi \approx 0°$ in the initial branch whereas $\phi \approx 180°$ in the desynchronization and galloping branches.

Barrero-Gil *et al.* (2009) reported that the critical Re for the onset of galloping of a square cylinder is $Re = 159$, i.e. galloping does not occur for $Re < 159$. Joly, Etienne & Pelletier (2012) found the same at $Re = 140$ for $m^* \leqslant 20$. Sen & Mittal (2015) identified a decrease in the critical Re from 186 to 169 with m^* increasing from 5 to 20. While a number of studies have been conducted so far on free vibrations of a square cylinder, investigations on the free vibration of two square cylinders in tandem are scarce. A few questions then arise. Could we extrapolate the knowledge of the single-cylinder response for the two cylinders? How does the response for two tandem cylinders behave in the two ranges of Re? How does the vibration response feature in the reattachment and coshedding flow regimes? The aim of this work is to investigate the free vibration response of a cylinder placed in the wake of a fixed cylinder. The distance between the cylinders is chosen as $L^* = 2$ and 6, lying in the reattachment and coshedding flow regimes respectively. Reynolds numbers of

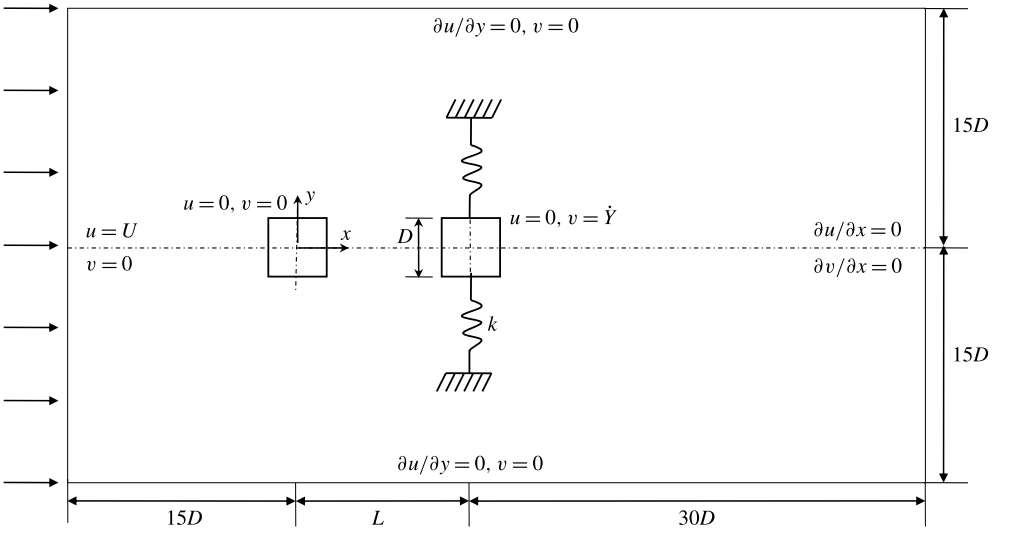

FIGURE 1. A schematic of the flow configuration and computational domain.

$Re = 100$ and 200 are chosen, which are respectively smaller and higher than the critical Re. The vibration and frequency responses, fluctuating lift (C_L'), phase lag between lift force and displacement, vortex shedding process, work done, wake structures and relationship between work done and flow structures are presented and discussed.

2. Problem description

Two cylinders of the same size are placed in a tandem arrangement in a rectangular computational domain. A schematic of the cylinder configuration is shown in figure 1. The upstream cylinder is stationary, while the downstream cylinder is spring mounted and allowed to oscillate in the transverse direction only. The stiffness of the spring is represented by k. All length quantities in the figure are presented in the scale of the cylinder width D. The Cartesian coordinate system is fixed in the domain, with the origin at the nominal centre of the upstream cylinder. The inlet boundary is $15D$ away from the upstream cylinder centre and the outlet is $30D$ away from the downstream cylinder centre. The upper and lower boundaries are symmetrically placed each $15D$ away from the centreline, giving a blockage ratio of 3.3 % (Zheng & Alam 2017). In order to encourage high-amplitude oscillation of the cylinder, the structural damping ratio ζ is set to zero (Sen & Mittal 2015). The mass ratio of the vibrating cylinder is $m^* = 3$. The values of Re are 100 and 200 based on D and the free-stream velocity U. At a given Re, the reduced velocity $U_r = U/(f_n D)$ is varied from 1 to 30 by changing the natural frequency f_n of the cylinder. Values of $L^* = 2$ and 6, corresponding to the reattachment and coshedding regimes respectively, are investigated.

2.1. *Governing equations and numerical methods*

The governing equations to simulate the flow field are the continuity and Navier–Stokes equations which can be written in non-dimensional form as

$$\nabla \cdot \boldsymbol{u} = 0 \tag{2.1}$$

and

$$\frac{\partial \boldsymbol{u}}{\partial t} + (\boldsymbol{u} \cdot \nabla)\boldsymbol{u} = -\nabla p + \frac{1}{\mathrm{Re}}\nabla^2 \boldsymbol{u}, \tag{2.2}$$

where $\boldsymbol{u} = (u, v)$ is the velocity field, p is the static pressure and t is the time. The D and U are considered as the reference length and velocity scales respectively for normalization.

The flow at the inlet is set uniform, $u = U$ and $v = 0$. Neumann conditions $\partial u/\partial x = 0$ and $\partial v/\partial x = 0$ are applied at the outlet. Free-slip boundary conditions ($\partial u/\partial y = 0$ and $v = 0$) are employed for the lateral boundaries, while no-slip conditions are imposed at the cylinder surfaces, $u = 0$, $v = 0$ for the stationary cylinder and $u = 0$, $v = \dot{Y}$ for the vibrating cylinder.

The governing equations (2.1) and (2.2) are solved for the unsteady and incompressible flow using the finite-volume-method-based software ANSYS-Fluent 15. The second-order upwind scheme is used to discretize the convective components and the central differencing scheme for diffusion terms. A first-order implicit formulation is adopted for the time discretization due to its unconditional stability (Manson, Pender & Wallis 1996) and compatibility with the dynamic mesh (Shaaban & Mohany 2018). The pressure-correction-based iterative algorithm SIMPLE (semi-implicit method for pressure linked equations) proposed by Patankar (1980) is employed for the coupling between the velocity and pressure fields.

The transverse dynamic response of the cylinder is governed by the following second-order ordinary differential equation in dimensionless form:

$$\ddot{Y} + 4\pi F_n \zeta \dot{Y} + (2\pi F_n)^2 Y = C_L/2m^*, \tag{2.3}$$

where $\ddot{Y}$, $\dot{Y}$ and Y are the instantaneous cross-flow acceleration, velocity and displacement of the cylinder respectively, with the Y measured from $y = 0$. Time is normalized by U and D. Here, C_L is the instantaneous lift coefficient of the cylinder and F_n $(= f_n D/U)$ is the normalized natural frequency of the cylinder. The cylinder mass ratio is defined as $m^* = m/\rho D^2$, where m is the mass of the cylinder per unit length and ρ is the density of the fluid. This second-order differential equation is solved using the fourth-order Runge–Kutta method for every time step.

A dynamic mesh scheme is utilized in the present study. The dynamic mesh model uses the ANSYS-Fluent 15 solver to move boundaries and/or objects and to adjust the mesh accordingly. The oscillating cylinder is surrounded by a grid box of size $2D \times 2D$ (figure 2*a*). The grid box moves with the vibrating cylinder, while the remaining grids in the domain are stationary. The interface is created by two parallel lines which separate the moving and stationary parts of the domain (figure 2*b*). The user defined function is incorporated into the solver for calculating the motion of the oscillating cylinder. At each time step, (i) the deformation of the domain is taken care of by the dynamic meshing tool in ANSYS-Fluent 15 and the mesh is updated using the Laplace smoothing method and (ii) equations (2.1) and (2.2) are solved and the lift force on the cylinder is obtained. The force is used to obtain the response of the oscillating cylinder using (2.3).

Structured grids are generated for the whole computational domain using the grid-generating software Gambit. Figure 2 displays the distribution of grids, with a total of 132 542 nodes for $L^* = 2$. The vibrating cylinder is positioned in a square region ($2D \times 2D$) enclosed by four interfacing lines that separate the moving and stationary regions. The square region moves with the vibrating cylinder and is given

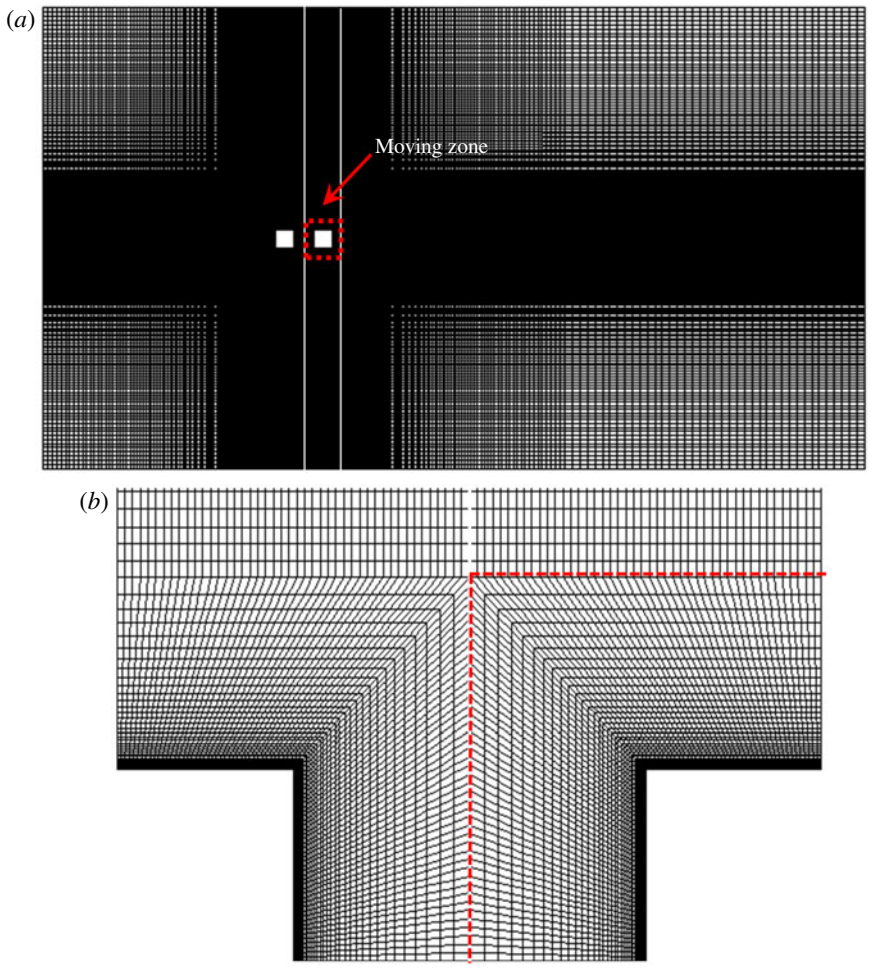

FIGURE 2. (Colour online) (*a*) Global view of the meshes around two cylinders at $L^* = 2$. (*b*) Zoomed-in view of the meshes around the cylinders.

a greater mesh density. The first level of the grid spacing near the cylinder wall is set at $0.008D$ away from the cylinder for an adequate resolution of the boundary layer. The grid spacing is then increased with an expansion rate of 1.05 in the normal direction. Following the same expansion factor in the same computation domain, the number of nodes for $L^* = 6$ is increased to 163 568.

Before conducting extensive simulations, grid and time-step independence tests were carried out for a single square cylinder. Following Sen & Mittal (2011), five different meshes in the range of 22 490–100 6152 were tested with $\Delta t = 0.01$, 0.008 and 0.005. Table 1 summarizes the Strouhal number St, time-mean drag coefficient $\bar{C}_D$ and fluctuating root-mean-square (r.m.s.) lift coefficient C'_L for the different meshes and time steps used. The percentage deviation with increasing number of nodes is indicated in brackets. The node number 50 350 is approximately half of the finest grid 100 612 considered here. The results are converged at mesh 50 350 and $\Delta t = 0.008$.

Time step	Number of nodes	St	C_L'	$\bar{C}_D$
0.01	22 490	0.154	0.263	1.486
	45 900	0.155 (0.65 %)	0.272 (3.30 %)	1.438 (3.22 %)
	50 350	0.157 (1.27 %)	0.263 (3.42 %)	1.466 (1.91 %)
	55 000	0.1565 (0.32 %)	0.265 (0.75 %)	1.46 (0.41 %)
	100 612	0.156 (0.31 %)	0.2646 (0.15 %)	1.457 (0.21)
0.008	22 490	0.153	0.256	1.493
	45 900	0.157 (2.54 %)	0.252 (1.56 %)	1.474 (1.27 %)
	50 350	0.159 (1.25 %)	0.247 (1.98 %)	1.45 (1.62 %)
	55 000	0.158 (0.63 %)	0.243 (1.61 %)	1.461 (0.75 %)
	100 612	0.157 (0.63 %)	0.246 (1.21 %)	1.452 (0.62 %)
0.005	22 490	0.157	0.258	1.504
	45 900	0.155 (1.27 %)	0.267 (3.37 %)	1.475 (1.92 %)
	50 350	0.158 (1.89 %)	0.254 (4.86 %)	1.469 (0.41 %)
	55 000	0.157 (0.63 %)	0.253 (0.39 %)	1.463 (0.41 %)
	100 612	0.156 (0.63 %)	0.252 (0.39 %)	1.459 (0.27 %)

TABLE 1. Grid- and time-step-independent study; $Re = 150$.

		$\bar{C}_D$	C_L'	St
$Re = 100$	Present	1.498	0.168	0.145
	Sohankar, Norberg & Davidson (1997)	1.477	0.156	0.146
	Robichaux, Balachandar & Vanka (1999)	1.530	—	0.1540
	Darekar & Sherwin (2001)	1.486	0.186	0.146
	Sharma & Eswaran (2004)	1.493	0.192	0.149
	Singh *et al.* (2009)	1.510	0.160	0.147
	Sahu, Chhabra & Eswaran (2009)	1.488	—	0.149
$Re = 200$	Present	1.479	0.351	0.172
	Saha, Biswas & Muralidhar (2003)	1.487	—	0.169
	Luo, Chew & Ng (2003)	1.451	—	0.165
	Sohankar, Norberg & Davidson (1999)	1.47	0.331	0.168
	De & Dalal (2006)	1.41	0.342	0.170

TABLE 2. Comparison of the results for a fixed single cylinder at $Re = 100$ and 200.

3. Result validation

Validation of the computational approach is provided here along with some benchmark results for a single and two cylinders. The simulated time-mean drag coefficient $\bar{C}_D$, fluctuating (r.m.s.) lift coefficient C_L' and Strouhal number St results for a single fixed cylinder at $Re = 100$ and 200 are compared with those in the literature in table 2. The comparison displays a good agreement.

Figure 3 displays a comparison of $\bar{C}_D$ acting on a pair of fixed cylinders at various values of L^* with results from Inoue, Iwakami & Hatakeyama (2006) and Sohankar (2012). While the present results accord well with those from Sohankar (2012), Inoue *et al.*'s (2006) results are underestimated, particularly for the upstream cylinder. A sudden jump in $\bar{C}_D$ for both cylinders is observed at $4.5 < L^* < 5$, distinguishing the reattachment (figure 3*c*) and coshedding (figure 3*d*) regimes.

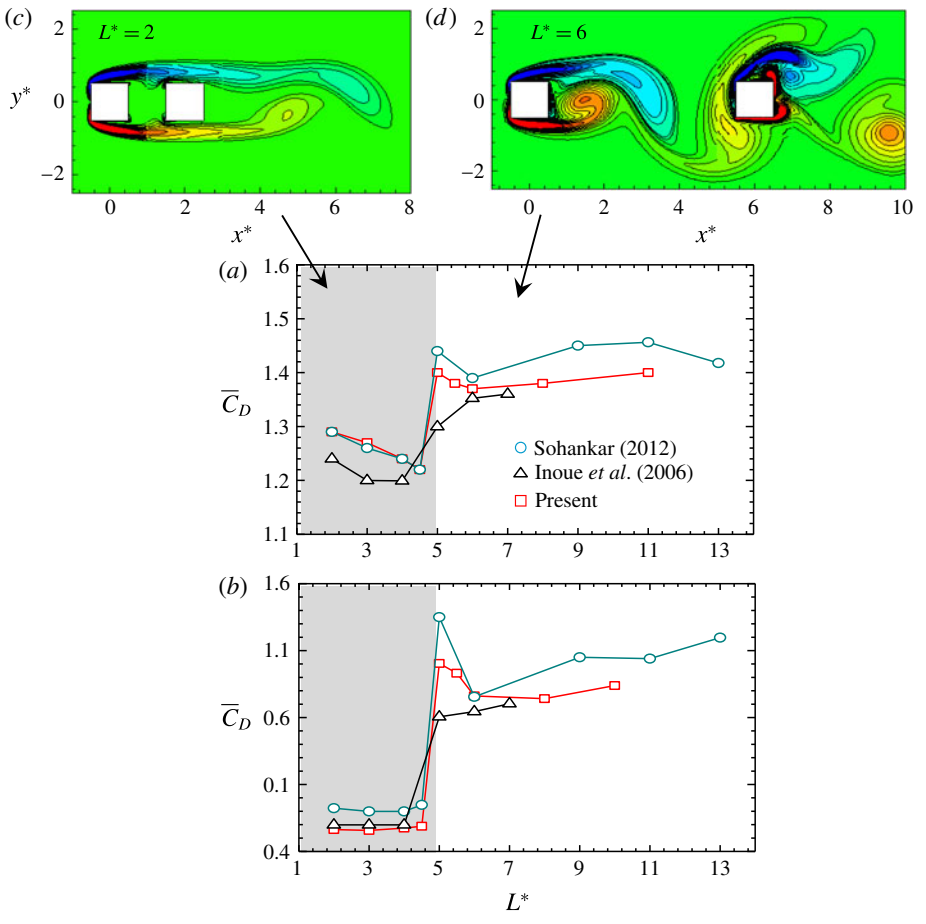

FIGURE 3. (Colour online) Comparison of time-mean drag coefficients for two cylinders at different values of L^* for $Re = 150$. (*a*) Upstream cylinder and (*b*) downstream cylinder. (*c*,*d*) Representative vorticity (ω_z^*) structures in the reattachment (shaded) and coshedding regimes respectively.

4. Single vibrating cylinder

The vibration response results for a single cylinder are presented in figures 4(*a*) and 5(*a*), showing the dependence of A^* on U_r at $Re = 100$ and 200. The A^* for the cylinder displacement Y is obtained by multiplying the r.m.s. value of Y by $\sqrt{2}$, i.e. $A^* = Y_{rms} \times \sqrt{2}$, which provides the average amplitude of the cylinder oscillation. The data of Zhao *et al.* (2013) for the same Re, m^* and ζ are also included in figure 4(*a*). The two curves have the same trend, validating our computations for the vibrating cylinder. The maximum amplitude is observed at $U_r \approx 5$ for either curve. Figure 4(*b–e*) displays vorticity structures at different values of U_r. In order to compare the timing of vortex shedding with respect to the cylinder displacement at different values of U_r, the vorticity structures are given for the cylinder at maximum displacement ($Y = Y_{max}$). As seen in figure 4(*a*), A^* is contingent on U_r. The cylinder response is divided into three regimes, namely the initial branch (IB), the lower branch (LB) and the desynchronization branch (DB), at $Re = 100$ (figure 4*a*). The different branches in the

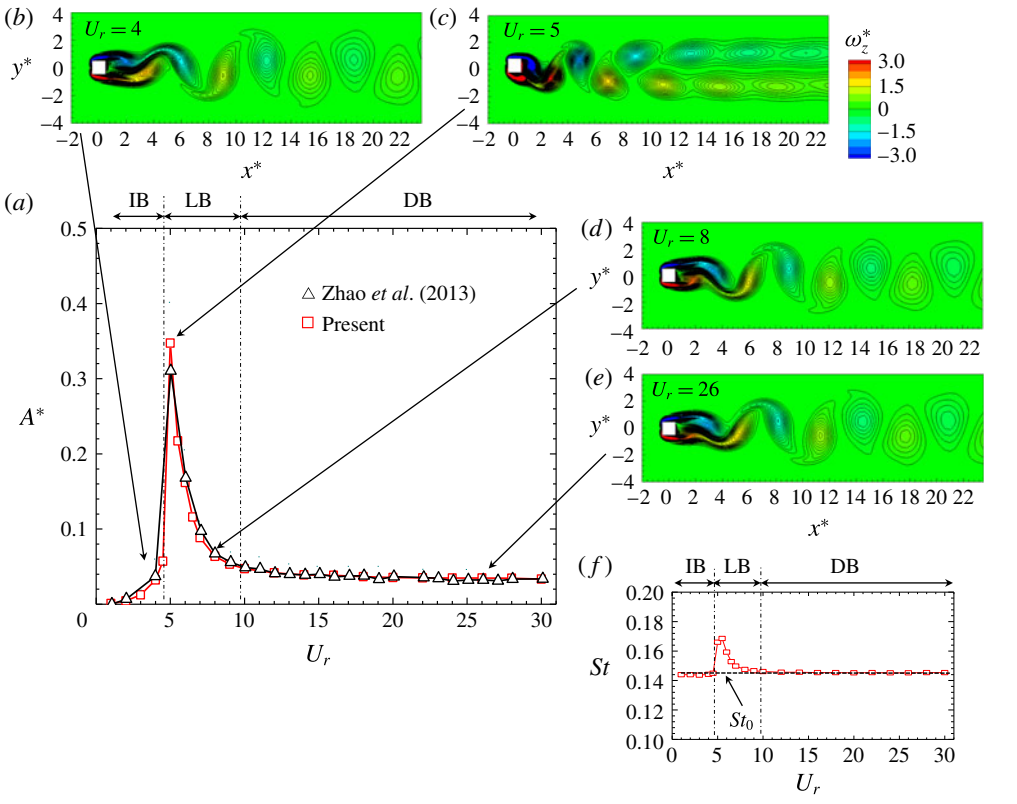

FIGURE 4. (Colour online) (*a*) Dependence on the reduced velocity U_r of the vibration amplitude A^* of a single cylinder. (*b–e*) Typical vorticity (ω_z^*) structures in different vibration regimes. (*f*) Dependence of the Strouhal number St on U_r. Here, $Re = 100$.

vibration response can be explored through the dependence of St on U_r (figure 4*f*). The Strouhal number was estimated from the power spectral density functions of the fluctuating lift forces. Given the fixed cylinder Strouhal number St_0 (figure 4*f*), it is observed that $St < St_0$ in the IB and $St > St_0$ in the LB, while $St \approx St_0$ in the DB. The initial branch occurring at $U_r < 4.5$ corresponds to A^* increasing with U_r. A drastic jump in A^* between $U_r = 4.5$ and 5.0 borders the IB and the LB, distinguished by a 2S vortex pattern before the jump (figure 4*b*) and a C(2S) vortex pattern after the jump (figure 4*c*). With the snapshots given for $Y = Y_{max}$, the growing shear layer appears over the upper surface of the cylinder in figure 4(*b*) and over the lower surface in figure 4(*c*) (Alam 2016). The timing of vortex shedding in the vorticity structures thus reflects that the phase lag between lift and displacement shifts from 0° to 180° between the IB and the LB (figure 4*b*,*c*). The phase lag was also confirmed from the results of cross-correlation between the lift and displacement. In the LB, A^* drops with increasing U_r, and the vorticity structure changes from C(2S) to 2S with the phase lag unchanged (figure 4*c*,*d*). The LB is followed by the DB, where A^* decays and reaches an asymptotic value. The streamwise separation between the vortices thus increases due to the desynchronization (figure 4*e*).

At $Re = 200$ (figure 5), a vortex excitation (VE) regime (including the IB and the LB) appears at $U_r \leqslant 12$, while the galloping branch (GB) crops up at $U_r > 12$. It will

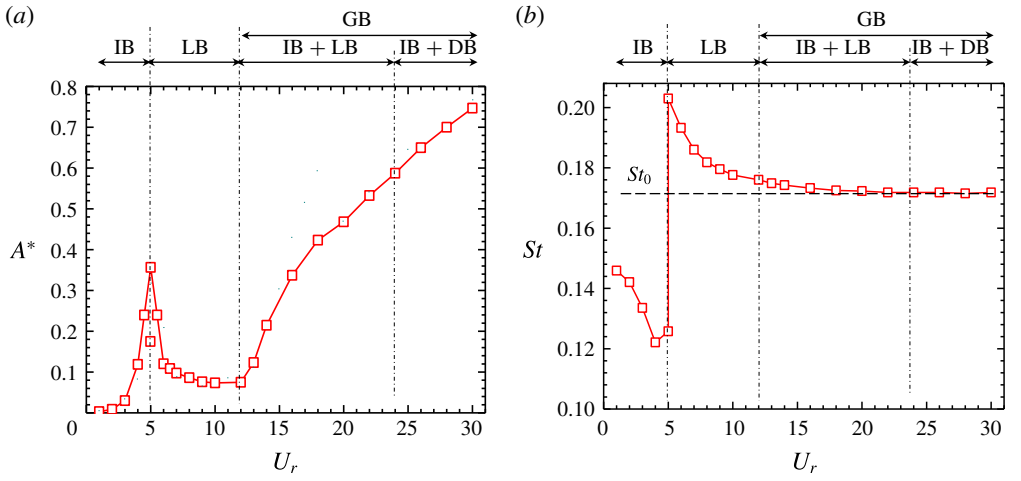

FIGURE 5. (Colour online) (*a*) Dependence on the reduced velocity U_r of the vibration amplitude A^* of a single cylinder. (*b*) Dependence of the Strouhal number St on U_r. Here, $Re = 200$.

be shown later that the vibration response at $12 < U_r < 24$ involves the characteristics of both the IB and the LB, and that at $U_r > 24$ the characteristics of both the IB and the DB. While the response characteristics at $U_r \leqslant 12$ in the VE regime are akin to those at $Re = 100$, the DB is postponed at $U_r > 24$ for $Re = 200$. There are two values of A^* as well as St at $U_r = 5$. It is a transition between the IB and the LB where the two flow modes corresponding to the IB and the LB appear intermittently. More information about the transition will be provided later. Again, $St < St_0$ at $U_r < 5$, indicating the IB. On the other hand, at $5 < U_r < 24$, $St > St_0$, which is an indication of the LB. The Strouhal number $St \approx St_0$ at $U_r > 24$, suggesting the DB. Therefore, the vortex shedding frequency characteristics conspicuously distinguish the IB and the LB. The value of A^* in the GB increases rather rapidly at $12 < U_r < 24$, and St decreases with U_r, reaching the asymptotic value at $U_r > 24$. Figure 6 presents the instantaneous vorticity contours along with the time histories of C_L and Y for $U_r = 3$, 4, 5, 9 and 20. Again, the vorticity snapshots are given for the same phase ($Y = Y_{max}$). The C_L and Y signals are in phase in the IB (figure 6a_1), and a 2S type vortex street materializes in the wake (figure 6a_2). For a value of U_r near the boundary between the IB and the LB, irregularity may occur in both signals (Navrose & Mittal 2017). At $U_r = 4$, the vortex shedding occurs in the 2S mode but the streamwise separation between two consecutive vortices differs (figure 6b_3). As such, a beat in the C_L and Y histories is discernible (figure 6b_1,b_2); the C_L as well as the Y amplitude is not constant, becoming large and small alternately following a period. Interestingly, a large peak corresponds to C_L leading Y (figure 6b_2), whereas C_L lags Y for a small peak. When C_L leads Y, positive work is done on the cylinder, which, gaining energy from the flow, can reach a large amplitude. On the contrary, when C_L lags Y, the gained energy of the cylinder is released into the flow (negative work); hence, the amplitude gets smaller. For $U_r = 5$, the C_L and Y signals comprise two intermittent modes (figure 6c). Between the two modes, the maximum amplitude of Y varies from 0.175 to 0.35 and that of C_L from 0.01 to 2.2. The high- and low-amplitude modes correspond to a low and a high oscillation frequency respectively (figure 6c_1). The flow mode associated with the high amplitude (figure 6c_1,c_2) is similar to the flow mode at $U_r = 4$ (figure 6b_3). For the small-amplitude mode (figure 6c_3), a double-row

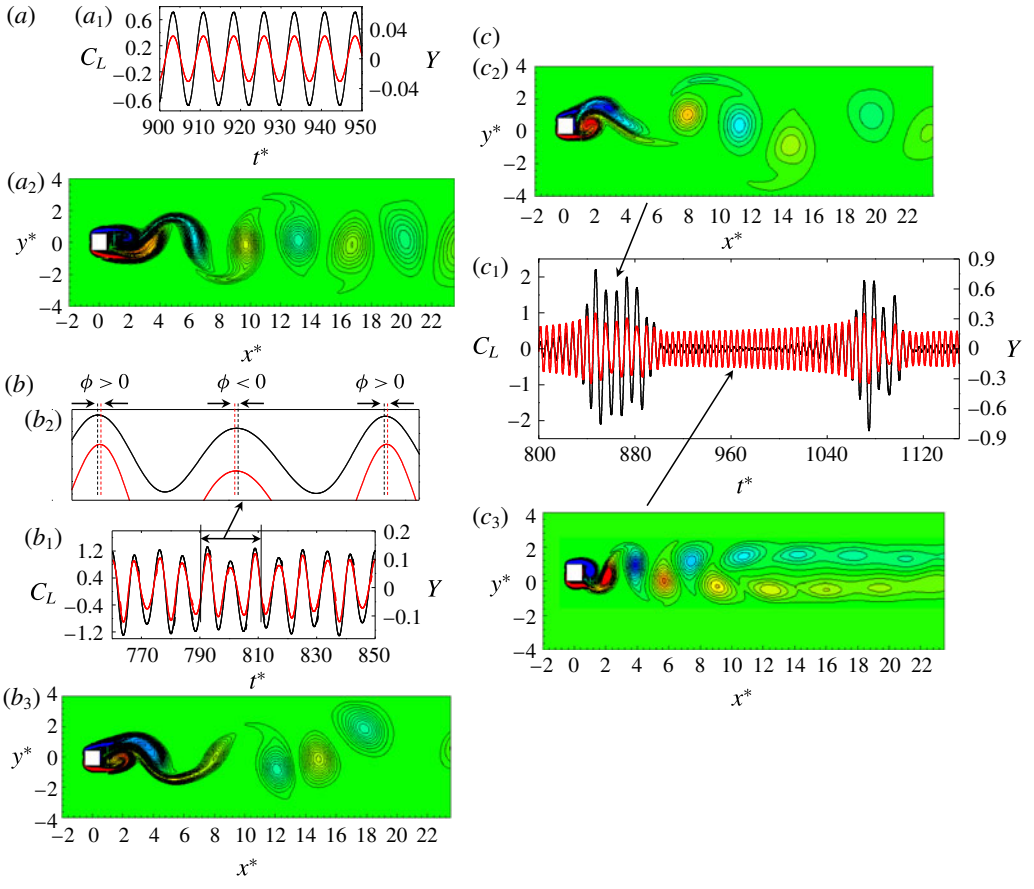

FIGURE 6. For caption see next page.

vortex street in the C(2S) mode characterizes the wake. The phase lag between C_L and Y is almost $\approx 0°$ and 180° in the large- and small-amplitude modes respectively. At $U_r > 5$, the phase lag is 180° (figure 6*d*).

Galloping is a structural instability phenomenon associated with a large amplitude and a low vibration frequency, prevailing for the non-circular cross-section (Blevins 1990). Presently, the galloping vibration occurs at $U_r > 12$ (figure 5*a*). Let us pay attention to the response and C_L signals at $U_r = 20$ (figure 6*e*) in the GB. Evidently, the predominant period of the cylinder oscillation is longer than the vortex shedding period (figure 6e_1), the oscillation frequency being smaller than the shedding frequency. Both the lift and the displacement signals are composed of low- and high-frequency components (figure 6e_1). These low- and high-frequency components were decomposed using the FFT-filter tool in the origin pro software. The cutoff frequency for the decomposition was chosen as the average of the high and low frequencies. The decomposed signals are presented in figure 6(e_2,e_3). Govardhan & Williamson (2000) and Ludlam, Gil & Velazquez (2017) decomposed the lift force into potential and vortex forces. The potential force is the inertia force due to the potential added mass. They obtained the potential force as the minus acceleration times the mass of the fluid displaced by the cylinder. The phase lag between the potential force and the displacement is thus 0° (inphase), and the frequency in the

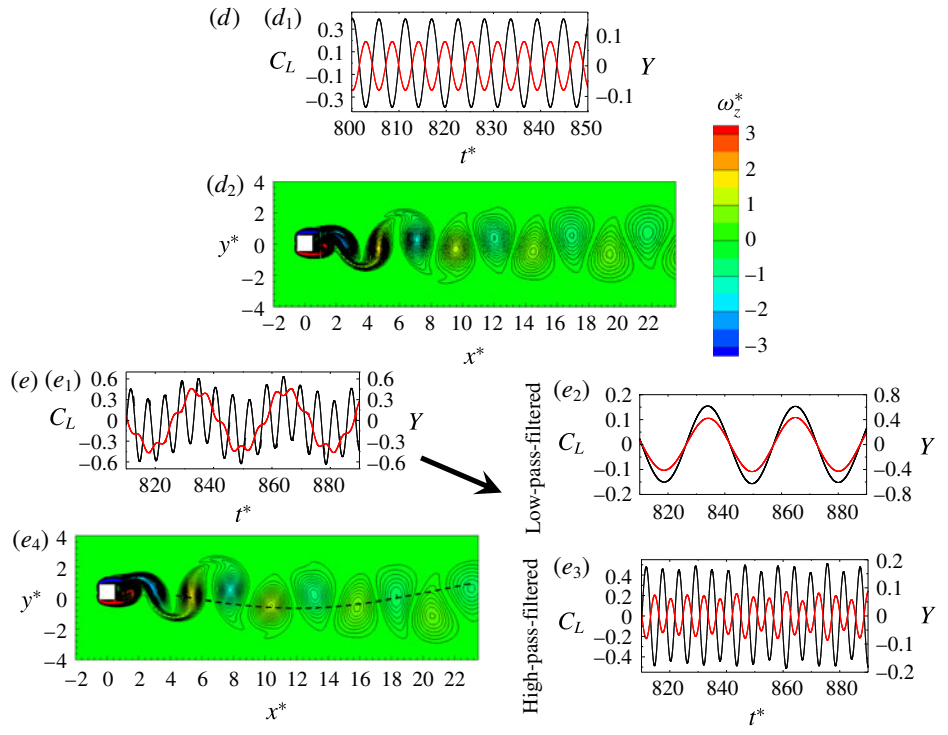

FIGURE 6. (cntd). (Colour online) Time histories of the lift force coefficient C_L (black lines) and the displacement Y (red lines), and representative vorticity (ω_z^*) structures for $U_r =$ (*a*) 3, (*b*) 4, (*c*) 5, (*d*) 9 and (*e*) 20. Here, $Re = 200$.

potential force is the same as that in the displacement signal. On the other hand, the frequency in the vortex force follows the vortex formation frequency. They used phase information on the forces to classify the different branches in the VE regime where the cylinder vibrates at one frequency. In the galloping regime of our study, the cylinder oscillates at two frequencies, corresponding to the cylinder natural frequency and the vortex shedding frequency. In order to get a clear phase relationship between the lift and the displacement, the signals of the lift and the displacement should have one identical frequency. Therefore, we decomposed the low- and high-frequency components of the lift and displacement signals in order to find the phase relationships between the lift and the displacement at low- and high-frequency components of oscillations separately.

Interestingly, the low- and high-pass-filtered C_L and Y signals (figure 6e_2,e_3) show that the low-frequency Y is dominant and in phase with the low-frequency C_L, the amplitude of which is very small. On the other hand, the high-frequency Y is small and antiphase with the corresponding C_L, having a high amplitude. That is, the high-frequency oscillation and shedding have characteristics similar to those in the LB, given $St > St_0$ (figure 5*b*) and the phase lag 180° between C_L and Y. The large-amplitude vibration associated with the low frequency is essentially the galloping vibration, bearing similar characteristics to those of the IB, given that $St < St_0$ and the phase lag is 0° between C_L and Y (figure 6e_2). The galloping vibration in $12 < U_r < 24$ is thus a combination of the IB and the LB, albeit A^* is predominantly associated with the former. At $U_r > 24$, the low-frequency C_L and Y do

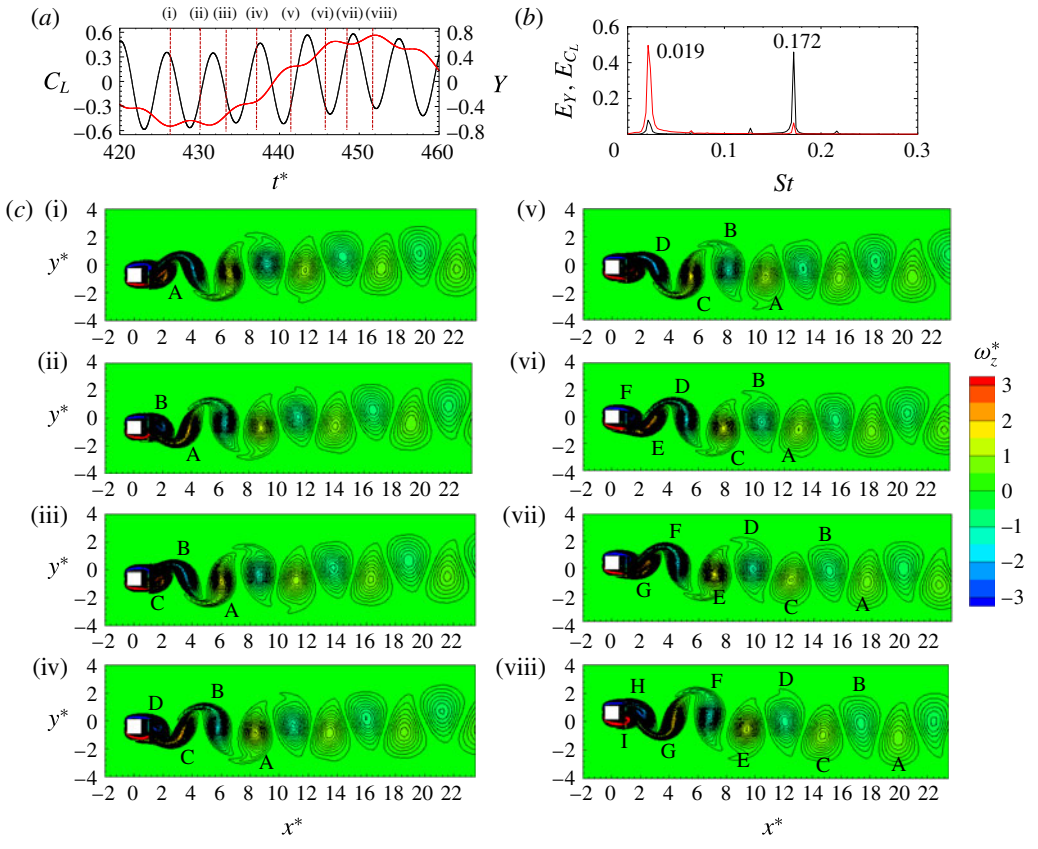

FIGURE 7. (Colour online) (*a*) Time histories of Y (red line) and C_L (black line). (*b*) Corresponding spectra. (*c*) Instantaneous vorticity (ω_z^*) contours at the timings marked at the top of (*a*). Here, $U_r = 30$ and $Re = 200$.

not differ from those at $12 < U_r < 24$, but the high-frequency C_L and Y correspond to $St \approx St_0$ (figure 5*b*). Thus, the galloping at $U_r > 24$ is a combination of the IB and the DB. Yet, the wake resembles 2S vortex streets (figure 7). It should be noted that the low-frequency C_L stems from the low-frequency wave (dashed line, figure 6e_4) of the vortex street following the cylinder oscillation. In summary, the galloping vibration resembles the IB in the sense that the predominant vibration amplitude grows with U_r, both following the same Y–C_L phase relationship.

Figure 7 shows the time histories of C_L and Y (figure 7*a*), the power spectra E_{CL} and E_Y for C_L and Y respectively (figure 7*b*), and the vortex structures (figure 7*c*) for a half cylinder-oscillation cycle for $U_r = 30$. The corresponding timing of each snapshot in figure 7(*c*) is marked by a vertical dashed line in figure 7(*a*). The C_L and Y histories each consist of a low and a high frequency. The low and high frequencies are dominant in Y and C_L respectively, as further evidenced by the power spectra in figure 7(*b*). The values of the dominant Strouhal numbers are 0.172 and 0.019 for C_L and Y respectively, suggesting that the vortex shedding occurs at $St = 0.172$ while the cylinder oscillation dominantly succeeds at $St = 0.019$. The vortex shedding and wake structures in figure 7(*c*) reveal that, as the cylinder moves from its bottom position to the top (instants (i–viii)), a total of nine vortices (marked as 'A'–'I') are formed (four

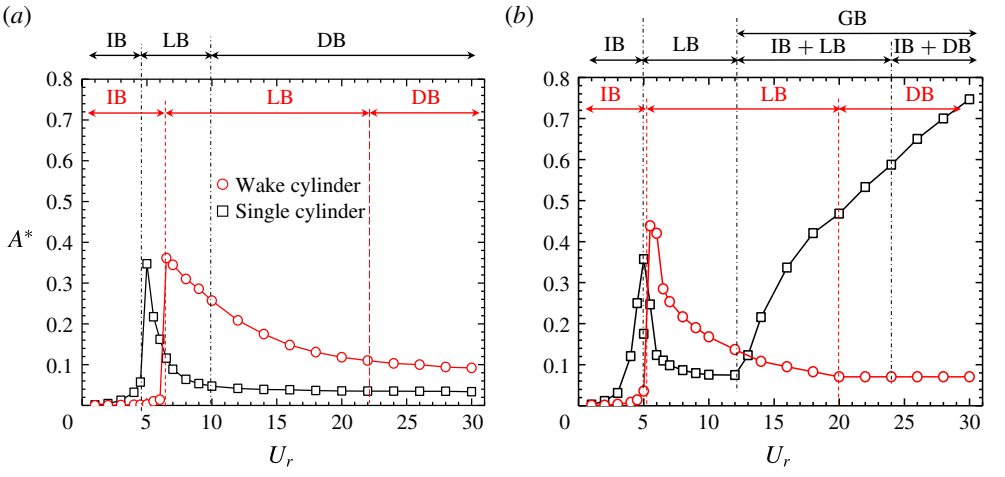

FIGURE 8. (Colour online) Variation in the vibration amplitude A^* with the reduced velocity U_r at (*a*) $Re = 100$ and (*b*) $Re = 200$. Here, $L^* = 2$.

from the upper side and five from the lower side) in a half cylinder-oscillation cycle. Similarly, when cylinder moves from the top to the bottom, another nine vortices come into being (not shown here). Therefore, the total number of shed vortices during an oscillation cycle is 18. This indicates that the vortex shedding mode is N(2S) (e.g. 9(2S) here), with the wake appearing similar to the 2S shedding mode.

5. Tandem cylinders

Here, results for the tandem cylinder case are presented at $L^* = 2$ and 6 for $Re = 100$ and 200, where the upstream cylinder is fixed and the downstream cylinder is free to vibrate.

5.1. *Reattachment regime ($L^* = 2$)*

5.1.1. *Vibration response*

Figure 8 shows the dependence of A^* on U_r at $Re = 100$ and 200. The single-cylinder response included in the figure distinguishes how the presence of the fixed upstream cylinder influences the response of the downstream cylinder. The downstream cylinder hereafter will be referred to as the wake cylinder. The vibration classifications given at the top of and in the figure are for the single and wake cylinders respectively. At $Re = 100$ (figure 8*a*), the IB is delayed for the wake cylinder compared with the single-cylinder counterpart. The delay is attributed to the shear-layer reattachment (figure 3*c*), which results in a smaller St for tandem fixed cylinders (Alam *et al.* 2002; Zheng & Alam 2018). A higher U_r is thus required to make $f_v = f_n$. The increase in A^* in the IB for the wake cylinder is very small compared with that for the single cylinder. The A^*, which is maximum at $U_r = 6.5$, reduces with an increase in U_r. The fashion of the reduction after the maximum A^* for the wake cylinder is, however, different from that for the single cylinder. The reduction for the single cylinder is rapid at $U_r = 5$–10 (LB regime) but slow at $U_r > 10$ (DB regime). The rapid reduction is, on the other hand, absent for the wake cylinder, the amplitude waning monotonically in a longer LB regime compared with

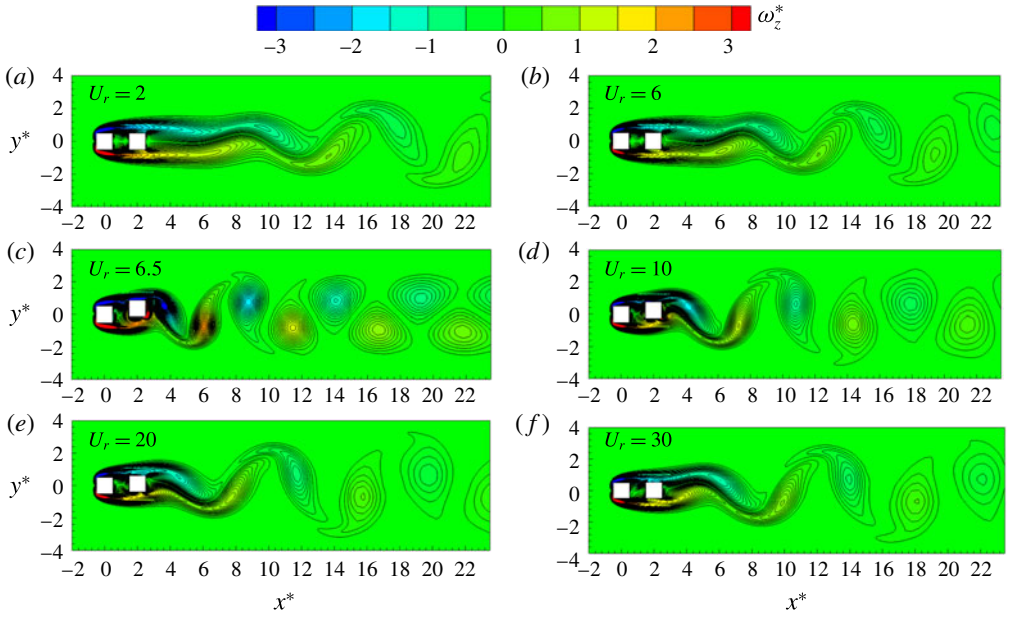

FIGURE 9. (Colour online) Instantaneous vorticity (ω_z^*) structures at various values of U_r. The instant of the snapshots corresponds to $Y = Y_{max}$. Here, $L^* = 2$ and $Re = 100$.

the single-cylinder counterpart. In the DB regime as well, A^* remains higher for the wake cylinder.

As Re is increased from 100 to 200 (figure 8*b*), the vibration response characteristics of the wake cylinder in the IB remain unchanged. The LB of the wake cylinder exhibits a rather more rapid decrease in A^* for $Re = 200$ than $Re = 100$. The U_r corresponding to the initiation (maximum A^*) of the LB decreases from $U_r = 6.5$ to 5.5 as Re is increased from 100 to 200. A further increase in U_r from the LB to the DB results in a gradual decay of A^* to be more or less constant at 0.07 at $U_r \geqslant 20$. For the single cylinder, the A^* drop is relatively sharp in the early stage of the LB, followed by A^* increasing in the GB regime ($U_r > 12$). Interestingly, although the single cylinder experiences galloping, the wake cylinder does not. That is, when the single cylinder at $Re = 200$ exhibits IB, LB and GB responses (figure 5*a*), the wake cylinder undergoes IB, LB and DB responses. The GB is absent for the latter. In addition, the U_r ranges of the different branches differ between the single and wake cylinders. These observations show that the knowledge on the single cylinder cannot be extrapolated for two cylinders. In the reattachment regime, the wake cylinder is encapsulated by the shear layers from the upstream cylinder. Due to the insufficient spacing between the cylinders and the shear layers largely reattaching on the side surfaces, the flow in the gap is small. The reattached shear layer may restrict the motion of the cylinder.

5.1.2. *Wake structures*

Figure 9 shows the instantaneous vorticity contours at different values of U_r for $Re = 100$. The vorticity structures correspond to the instant $Y = Y_{max}$. For the IB (figure 9*a*,*b*), the two shear layers separating from the upstream cylinder reattach almost steadily on the wake cylinder, forming a quasisteady flow region in the gap

between the cylinders. Vortices shed only from the wake cylinder. With an increase in U_r from 2 to 6, the roll-up of the vortices shifts upstream, indicating that the formation length shrinks. The wake cylinder is encapsulated by the shear layers from the upstream cylinder. Due to this encapsulation, the fluctuating lift force on the wake cylinder is reduced compared with that on the single cylinder, leading to a small value of A^* in the IB regime for the wake cylinder (figure 8*a*). Comparing the fluctuating lift and the maximum amplitude of the downstream cylinder, Alam & Kim (2009) and Kim *et al.* (2009), for two circular cylinders, concluded that the maximum amplitude of the downstream cylinder follows the fluctuating lift measured on the stationary downstream cylinder. Qin, Alam & Zhou (2017), for two tandem circular cylinders of different diameters, found that an increase in A^* results from an increased fluctuating lift when the phase lag between Y and C_L does not change much, or when the inertia force is small due to small amplitude and frequency (Govardhan & Williamson 2000). The phase lag between the lift and the displacement is 0°, as can be seen from the timing of vortex shedding at $Y = Y_{max}$ (figure 9*a*,*b*). With an increase in U_r from the IB to the LB (figure 9*c*), the flow in the gap becomes unsteady, as the two upstream-cylinder-generated shear layers reattach alternately on the upper and lower side surfaces of the wake cylinder. The phase lag becomes 180°. The longitudinal spacing between two consecutive vortices becomes small. The small spacing between two consecutive vortices can be ascribed to the increased St from the IB to the LB (figure 4*f*). An increased St means that a vortex has a shorter time to convect downstream before the next vortex coming into the street and *vice versa*. As A^* decays from $U_r = 6.5$ to 20 (figure 8*a*), the shear-layer rolling is postponed and the streamwise separation between the vortices is elongated (figure 9*c–e*). Again, the elongated separation between the vortices is linked to the decrease in St with U_r (figure 4*f*). In the DB regime, where A^* is small, a further postponement in the shear-layer rolling takes place (figure 9*f*).

Figure 10 shows the instantaneous vorticity contours at $Re = 200$. A similar observation is made for the IB (figure 10*a*,*b*) as made for $Re = 100$ (figure 9*a*,*b*). The vortex shedding, however, occurs closer to the cylinder at $Re = 200$ than at $Re = 100$. The wake is characterized by the 2S mode. A C(2S) mode appears at $U_r = 5.5$ (figure 10*c*) where A^* is maximum in the LB. However, as U_r is increased, the wake turns into a 2S mode (figure 10*d*,*e*). In the DB, the vortex formation length and streamwise separation between vortices are both elongated (figure 10*f*).

5.1.3. *Frequency response*

Figure 11 presents variations in the vibration frequency ratio f^* $(=f_0/f_n)$, where f_0 is the cylinder-oscillation frequency extracted from the power spectral density function of Y. The values f_0 were taken as the frequencies corresponding to the dominant peaks in the power spectral density function. Let us first compare the f^* of the wake cylinder with that of the single cylinder at $Re = 100$. The f^* in the IB is slightly smaller for the wake cylinder than for the single cylinder. In the IB and LB regimes, the relationship between f^* and U_r is nonlinear, different from an $St = St_0$ or $St = St_{0w}$ relationship (figure 11*a*), where St_0 and St_{0w} are the Strouhal numbers of the fixed single and fixed wake cylinders respectively. The Strouhal numbers in both regimes thus differ from St_0 (figure 4*f*) or St_{0w}, albeit the difference is very small for the wake cylinder in the IB as A^* is small. Modifying from the natural vortex shedding frequency (fixed cylinder), the vortex shedding frequency of the oscillating cylinder locks in with the oscillation frequency. Khalak & Williamson (1999) suggested that f^* may be much higher or smaller than unity for a smaller m^*; therefore, the lock-in may be defined based on the

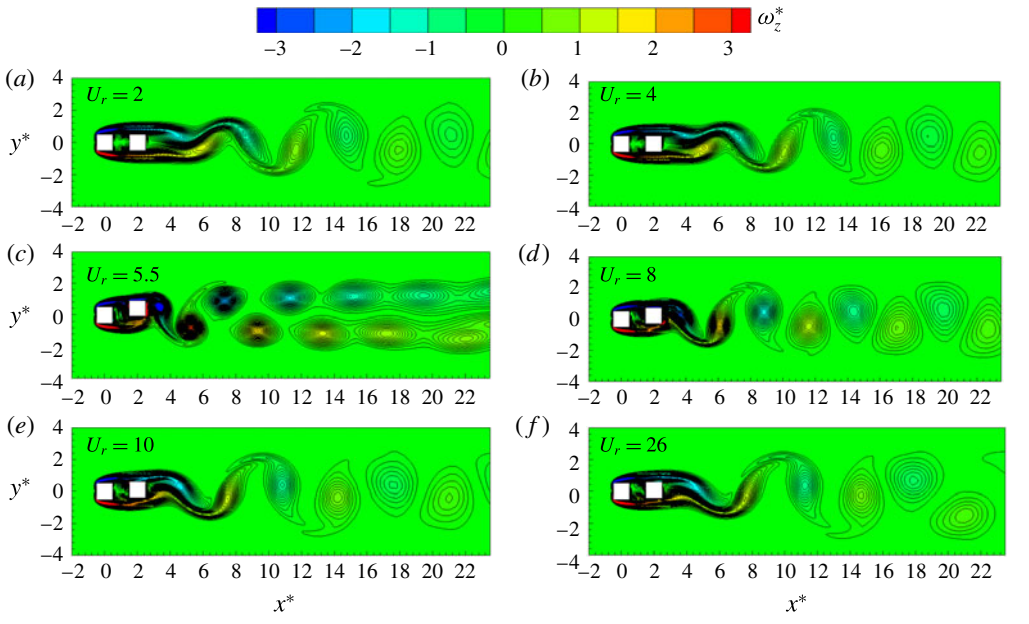

FIGURE 10. (Colour online) Instantaneous vorticity (ω_z^*) structures at different values of U_r. The instant of the snapshots corresponds to $Y = Y_{max}$. Here, $L^* = 2$ and $Re = 200$.

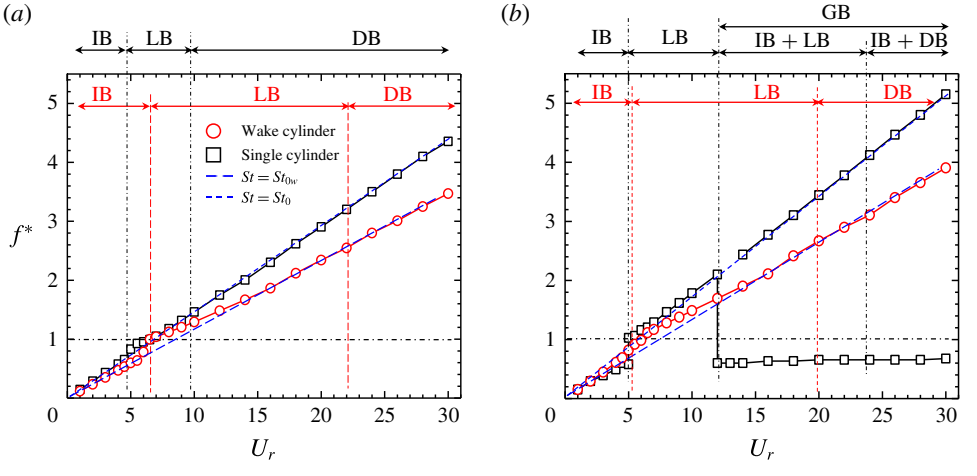

FIGURE 11. (Colour online) Variation in the oscillation frequency ratio f^* ($=f_0/f_n$) with the reduced velocity U_r at (*a*) $Re = 100$ and (*b*) $Re = 200$. Here, St_0 and St_{0w} represent the Strouhal numbers of the fixed single and wake cylinders respectively and $L^* = 2$.

synchronization of the vortex shedding frequency with the vibration frequency. In the DB regime, the f^*–U_r relationship is linear, following $St = St_0$ for the single cylinder and $St = St_{0w}$ for the wake cylinder.

A significant change takes place when Re is increased to 200 (figure 11*b*). For the single cylinder at $U_r = 5$, there are two f^* values, $f^* = 0.58$ and 1.01, corresponding to the IB (2S) and LB (C(2S)) modes respectively. For $5 < U_r \leqslant 12$, a single value

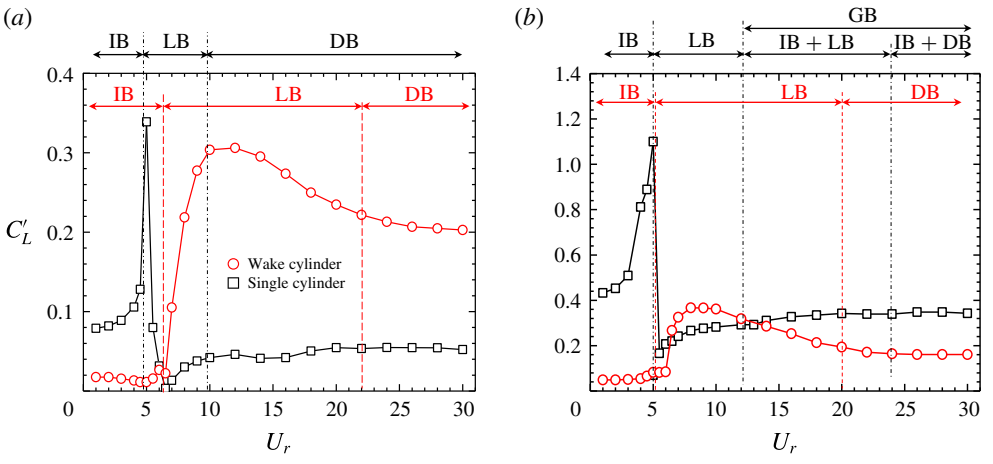

FIGURE 12. (Colour online) Variation in the fluctuating (r.m.s.) lift coefficient C'_L with reduced velocity U_r at (*a*) $Re = 100$ and (*b*) $Re = 200$. Here, $L^* = 2$.

of f^* is seen, where the oscillation and shedding frequencies are the same. On the other hand, there are two values of f^* for $U_r > 12$ (GB) where the cylinder oscillation has two frequencies (figure 6*e*), corresponding to the shedding frequency (close to the $St = St_0$ line) and a modified natural frequency ($f^* < 1.0$). The value of $f^*(<1.0)$ increases very slightly from 0.60 to 0.67 in the range $U_r = 12$–30 examined. The vibration amplitude at the shedding frequency is much smaller compared with that at $f^* < 1.0$ (figure 6*e*). The set of $f^* < 1.0$ is predominant, at which the cylinder vibrates predominantly. This justifies the presence of the LB and the DB in the GB. For the wake cylinder, the high-frequency f^*–U_r relationship differs from $St = St_{0w}$ in the IB and the LB, but coincides in the DB.

5.1.4. *Fluctuating lift force*

Figure 12(*a*) shows C'_L for both the single and the wake cylinders at $Re = 100$. The C'_L of the single cylinder in the IB rises exponentially with U_r, attaining a peak at $U_r = 5$ where A^* is maximum (figures 12*a*, 4*a*). The C'_L in the LB plunges between $U_r = 5$ and 6.5 where A^* rapidly decays. The plunge is attributed to f^* approaching 1.0 (figure 11*a*). On the other hand, C'_L grows slowly for $U_r > 6.5$ where the decay in A^* occurs at a very small rate and f^* departs from $f^* = 1.0$. The change in C'_L is relatively small in the DB regime. For the wake cylinder, the C'_L is more or less constant in the IB (following A^* in figure 8*a*), while it increases rapidly from $U_r = 6.5$ to 12 in the LB and decreases for $U_r > 12$. Again, a small drop in C'_L between $U_r = 6.0$ and 6.5 is attributed to the f^* becoming 1.0 (figure 11*a*). The C'_L variations of the single and wake cylinders are opposite to each other for $U_r > 10$, although A^* for the two cases follows similar trends.

The variation in C'_Lin the IB and the LB at $Re = 200$ (figure 12*b*) is similar to that at $Re = 100$. For $U_r > 12$ where galloping vibration occurs for the single cylinder, the C'_L of the single cylinder surpasses that of the wake cylinder. With increasing U_r (> 20), the wake cylinder C'_L approaches a constant value ($C'_L = 0.16$) that is 52 % smaller than that of the single cylinder C'_L ($= 0.34$).

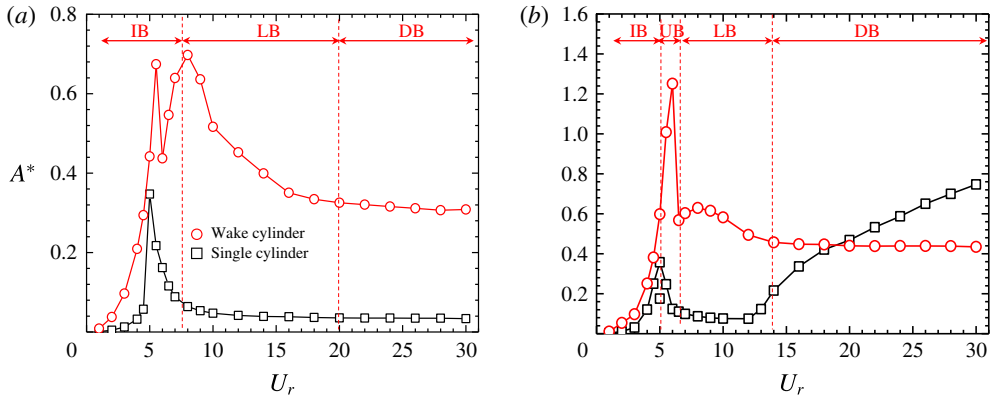

FIGURE 13. (Colour online) Variation in the amplitude A^* with the reduced velocity U_r at (*a*) $Re = 100$ and (*b*) $Re = 200$. Here, $L^* = 6$.

5.2. *Coshedding regime* ($L^* = 6.0$)

5.2.1. *Vibration and frequency responses*

The dependence on U_r of the wake cylinder A^* at $L^* = 6.0$ is shown in figure 13 for $Re = 100$ and 200. The response regimes are marked only for the wake cylinder. The boundaries between different branches are identified based on St, f^* and the phase lag between Y and C_L. All follow the same relationships between themselves and branches as stated for the single cylinder. At $Re = 100$, the A^* of the wake cylinder is much higher in all three branches compared with that of the single cylinder. Furthermore, the variation in A^* is different from that at $L^* = 2.0$ (figure 8). The A^* increases exponentially with U_r, reaching a peak ($A^* = 0.67$) at $U_r = 5.5$, the peak value being approximately two times greater than the single cylinder A^* at $U_r = 5$ (figure 13*a*). Another peak forms in the LB regime at $U_r = 8$. The enhancement in A^* of the wake cylinder compared with the single cylinder can be ascribed to the interaction of the upstream-cylinder-generated gap vortices with the wake cylinder. The A^* in the DB is approximately 12 times that of the single cylinder and three times that of the wake cylinder at $L^* = 2.0$. The transition from the IB to the LB is accompanied by a shift in the phase lag from 0° to 180° (to be shown later) and by a change in St from $St < St_w$ to $St > St_w$ (figure 14*a*). On the other hand, $St > St_w$ and $St = St_w$ distinguish the LB and DB at $U_r = 20$.

At $Re = 200$ (figure 13*b*), the response amplitude is very similar to the single-cylinder case for $U_r < 5.0$ (IB). The A^*, increasing with U_r, reaches a value of 1.25 at $U_r = 6$, followed by a sudden drop at $U_r = 6.5$. As will be shown later, $5.0 < U_r < 6.5$ represents the upper branch (UB) which is followed by the LB ($6.5 < U_r < 14$) and then the DB ($U_r > 14$). The phase lag between C_L and Y is approximately 0° in the IB and the UB, and suddenly switches to 180° in the LB. At $Re = 200$, the UB and IB have the same characteristics in terms of the phase lag between C_L and Y and of the relationship between St and St_w (figure 14*b*). The vortex shedding mode, however, changes from a 2S at the IB to a (P + S)-like vortex arrangement at the UB, which will be shown later in § 5.4. Interestingly, no galloping vibration is observed for the wake cylinder at this Re, although it is observed for the single cylinder at $U_r > 12$. It is quite different from a circular cylinder. A single circular cylinder generally

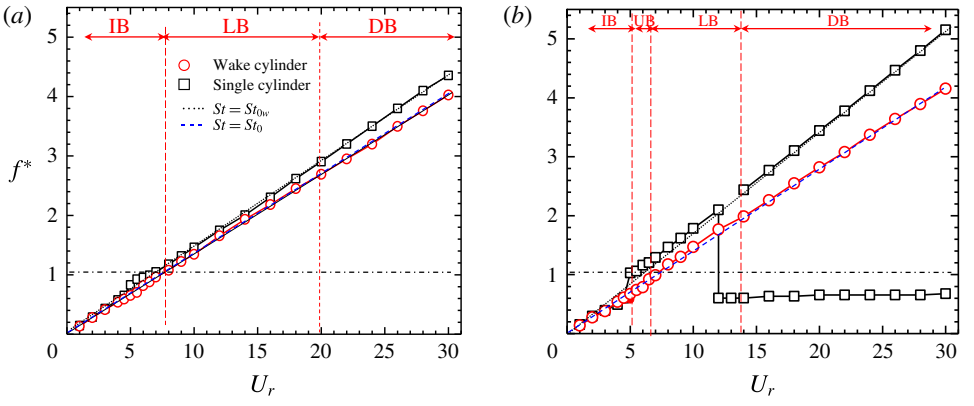

FIGURE 14. (Colour online) Variation in the oscillation frequency ratio $f^*(=f_0/f_n)$ with the reduced velocity U_r at (*a*) $Re = 100$ and (*b*) $Re = 200$. Here, St_0 and St_{0w} represent the Strouhal numbers of the fixed single and wake cylinders respectively and $L^* = 6$.

does not experience galloping vibration, but a wake circular cylinder does (Kim *et al.* 2009; Assi, Bearman & Meneghini 2010; Alam & Meyer 2013; Qin *et al.* 2017). The opposite is true for square cylinders: galloping occurs for the single cylinder but not for the wake cylinder for the values of L^* examined. It is expected that, for a sufficiently large value of L^*, the wake cylinder will behave like an isolated cylinder, and galloping may come into being for the wake cylinder.

Recently, VIV of cylinders has received more attention because of its use as a source of energy harvesting. Mehmood *et al.* (2013), at $96 \leqslant Re \leqslant 118$, investigated the concept of harvesting energy from VIV of a circular cylinder by attaching a piezoelectric transducer. They reported that the load resistance influences the oscillation amplitude, lift coefficient and harvested power. An increase in the load resistance widens the synchronization regime. Maruai *et al.* (2018) numerically examined the transverse vibration of a square cylinder at $Re = 3.6$–12.5×10^3 for $m^*\zeta = 2.48$. They introduced a downstream flat plate in the wake of a cylinder with gap spacing ratios of 0.1–3 and observed a large-amplitude vibration at a gap ratio of 0.1 where the power harvested was maximum. Presently, it is observed that the vibration amplitude of the wake cylinder is mainly dominated by the interaction between the gap vortices and the wake cylinder. The gap vortex may play an essential role in the energy transfer from the fluid to the cylinder, sustaining the high-amplitude vibration at $L^* = 6$. The vibration amplitude at $L^* = 6$ is remarkably enhanced compared with the cases of $L^* = 2$ (figures 8 and 13) and a single cylinder (figure 13) except for $U_r > 18$ at $Re = 200$ (figure 13*b*). Interestingly, the wake cylinder at $L^* = 6$ can be of a source of energy harvesting where the flow velocity is low.

5.2.2. *Wake structure*

In the previous section, quite a few interesting observations were made, for example the formation of two peaks in A^* at $Re = 100$ and the presence of an UB at $Re = 200$. We can gain insight into these phenomena through vorticity structures, vortex shedding process and work done on the cylinder by the fluid.

5.3. *Wake structure at different branches of vibration at* $Re = 100$

5.3.1. *Wake structure and phase relationship between* C_L *and* Y

Figure 15 shows vorticity structures and time histories of C_L and Y at different values of U_r. Each snapshot corresponds to the instant at which the wake cylinder is at the bottom position ($Y = -Y_{max}$). The wakes at $U_r = 1.0$ and 4.0 feature the 2S mode while that at $U_r = 5.5$ is characterized by the C(2S) mode where A^* is maximum in the IB. The gap vortices vigorously interact with and impinge on the wake cylinder. Both the C_L and Y amplitudes grow with increasing U_r from 1.0 to 5.5. Between $U_r = 5.5$ and 6 where A^* drops, C_L declines, and the C(2S) wake transmutes to the 2S wake (figure 15*c*,*d*). The impinging vortex A on the lower surface (figure 15*c*) dictates the shedding and C_L, and its timing leads to an increase in C_L at $U_r = 1.0$–5.5 and a drop at $U_r = 5.5$–7.0. The upper gap vortex B gets closer to the upper leading edge with increasing U_r from 5.5 to 7.0, which is another reason why C_L is reduced. At $U_r = 7.0$, the gap vortex B impinging on the leading edge enhances the growth of the shear layer on the upper surface under an impulse (see the zoomed-in view). The mechanics enhances the upward lift force; the vortex B impinging on the upper surface of the wake cylinder at $U_r = 8$ makes the C_L positive and the phase lag 180° between C_L and Y. One can see in the zoomed-in views that two small shear layers form very close to the upper and lower surfaces respectively (figure 15*f*, zoomed-in view). They have a greater impact on C_L as they are close to the cylinder. The vortex B also impinges on the upper surface. Therefore, the shear layers and vortex impingement result in a modification in C_L. The shear-layer shedding and associated lift are connected to the motion of the cylinder, in phase and antiphase with Y in the IB and LB regimes respectively, while the impingement-induced lift is contingent on U_r, as can be confirmed from the C_L and Y histories. The shear-layer-induced vortex and impingement vortex form a binary vortex behind the cylinder, which results in a 2S wake. One question may arise as to why A^* increases and C_L decays with U_r increasing from 5.5 to 8. The point is that there is a phase lag between the upper shear-layer growth and the impinging vortex B (figure 15*c*–*f*). As such, vortex B leads the shear layer at $U_r = 6$, is in phase with the shear layer at $U_r = 8$ and lags the shear layer at $U_r = 10$. This explains why A^* increases between $U_r = 6$ and 8, but declines for $U_r > 8$.

5.3.2. *Vortex shedding process and work done*

Here, we will explain the vortex shedding process at $U_r = 8$ where A^* is maximum in the LB. Figure 16 presents the mechanism of the vortex shedding process in one oscillation period. The (i), (ii), (iii), etc., given at the upper-left corners of the snapshots, represent the timings marked at the top of the time histories of Y and C_L in figure 17(a_1). Obviously, C_L and Y are almost antiphase (figure 17a_1). At instant (i), the cylinder is at its bottom position. A negative-vorticity shear layer separating from the upper leading edge of the wake cylinder reattaches on the trailing edge, forming a separation bubble and generating a vortex C_1 (figure 16(i)). The shear-layer separation, reattachment and bubble formation can be clearly viewed in figure 16(i). The gap vortex B_1 lies on the upper side surface of the wake cylinder. While the separation bubble, causing a highly negative pressure on the upper surface, results in the upward directed lift maximum, the impinging B_1 weakens the growth of the shear layer and reduces the lift, forming a kink (figure 17a_1) in C_L around instant (i). When the cylinder moves upward (instants ii, iii), vortices B_1 and C_1 form a binary vortex $B_1 + C_1$ that gets saturated at instant (iii) and completes its shedding at instant (iv) where the lower shear layer forms a separation bubble. Vortex B_2 impinges on the

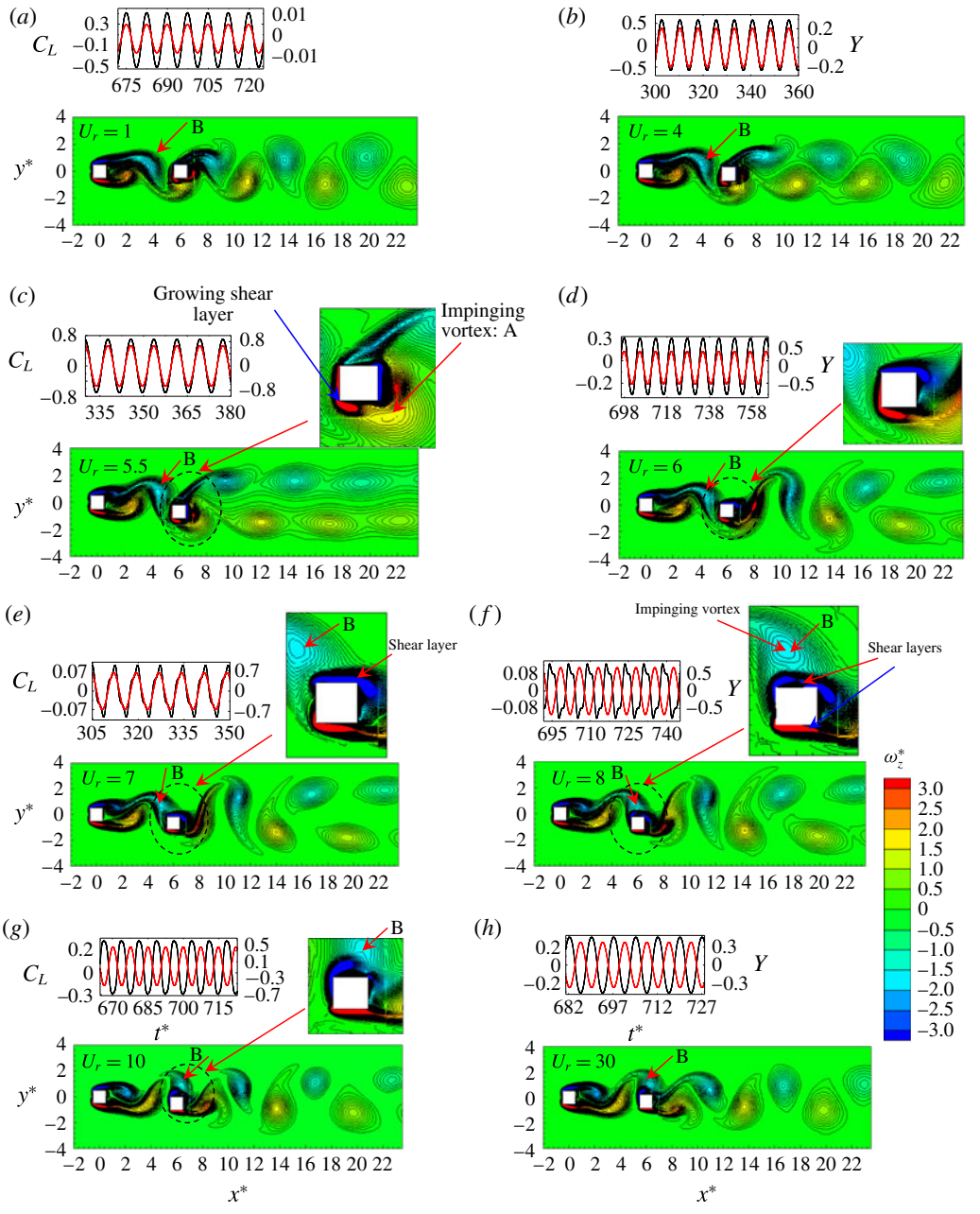

FIGURE 15. (Colour online) Instantaneous vorticity (ω_z^*) structures and time histories of the lift force C_L (black lines) and displacement Y (red lines) at various values of U_r. The instant of the snapshots corresponds to $Y = -Y_{max}$. Here, $L^* = 6$ and $Re = 100$.

lower corner at instant (iii) and restricts the growth of the shear layer at instant (iv), forming another kink in C_L (figure 17a_1). Between instants (iv) and (vi), the cylinder moves downward and the binary vortex $B_2 + C_2$ forming from B_2 and C_2 completes its shedding (figure 16iv–vi). This observation confirms a 2S mode. It is thus clear

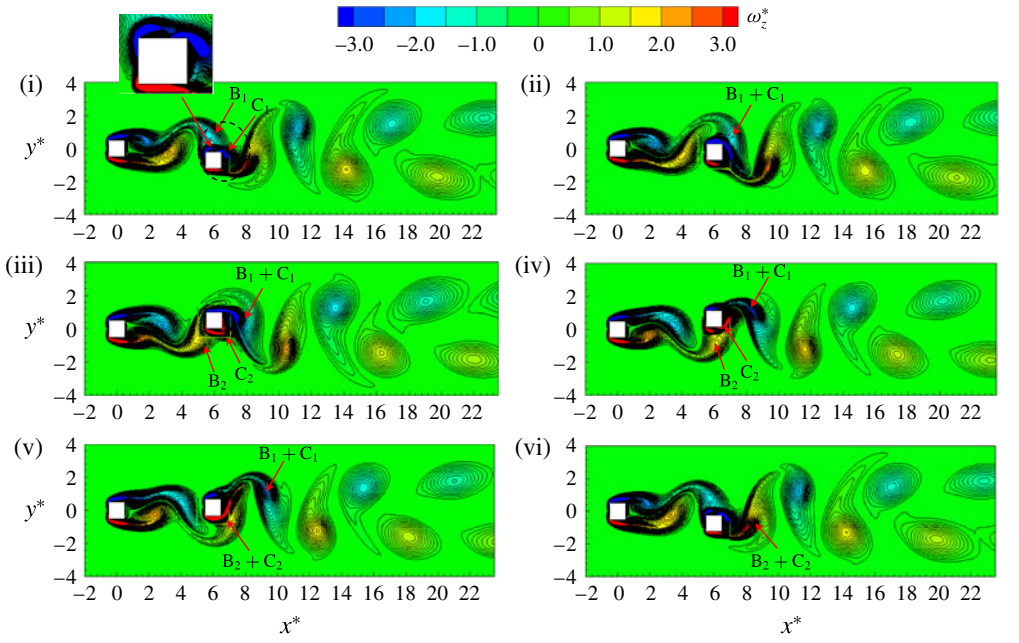

FIGURE 16. (Colour online) Instantaneous vorticity (ω_z^*) structures in one period of oscillation. The instants marked at the top left corners of the snapshots correspond to the timings marked at the top of figure 17(a_1). Here, $U_r = 8$, $L^* = 6$ and $Re = 100$.

that, in one period of the vortex shedding, two impinging vortices form two kinks in the C_L history, having a frequency of twice the oscillation frequency.

The vortex shedding from the upper and lower sides of the cylinder (figure 16(i,iv)) leads to a variation in C_L following the vortex shedding frequency. On the other hand, the gap-vortex impingement occurs twice in one vortex shedding cycle, leading to a variation in C_L at a frequency of twice the shedding frequency. The C_L thus constitutes a low frequency (shedding frequency) and a high frequency (impinging frequency), the former being the same as the oscillation frequency. In order to see the C_L amplitude corresponding to the cylinder-oscillation frequency and vortex impingement frequency, low- and high-pass-filtered C_L histories are presented in figure 17(a_2). The cutoff frequency was 1.5 times the cylinder-oscillation frequency. Obviously, the C_L amplitude induced by the impingement is smaller than that by the vortex shedding from the cylinder. The vortex-shedding-induced C_L is positive and negative (instants (i, iv), figure 17a_2) when the vortex shedding occurs from the upper and lower sides respectively (figure 16(i,iv)). Interestingly, when the gap vortex B_1 impinges near the leading edge of the cylinder (figure 16(i)), the associated C_L (i.e. high pass) is negative (figure 17a_2). As it passes over the trailing edge (figure 16(ii)), the associated C_L becomes positive (instant (ii) in figure 17a_2). The C_L associated with the shedding is antiphase with Y while that associated with the impingement is almost in phase with Y, considering the peak-to-peak phase. The latter is thus responsible for the large A^*.

It is worth seeing the work done by the vortex shedding and impingement. Figure 17(b) shows time histories of work done W ($= C_L \, \mathrm{d}Y$) by the vortex-shedding-induced C_L (low pass), impingement-induced C_L (high pass) and the total C_L. The work done fluctuates from positive to negative and *vice versa* for all three cases. This

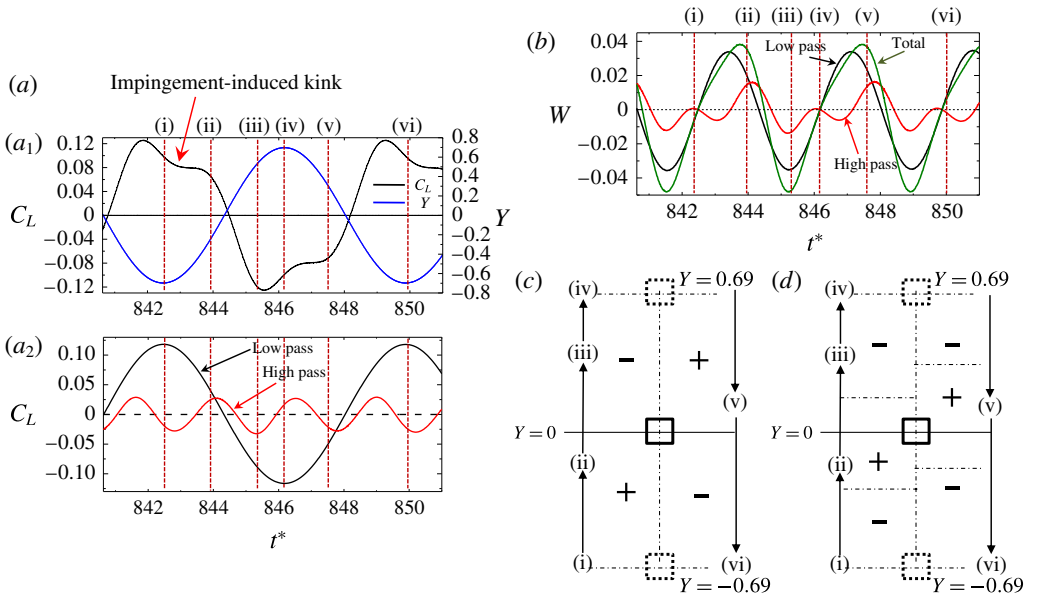

FIGURE 17. (Colour online) (*a*) Time histories of Y, C_L and filtered C_L. (*b*) Temporal variation of total work done and filtered work done. (*c*,*d*) Sketch for the signs of the work done by vortex shedding and vortex impingement respectively in one cycle of the cylinder oscillation. The instants marked at the top of figure 17(a_1) correspond to the snapshots in figure 16. Here, $U_r = 8$, $L^* = 6$ and $Re = 100$.

means that the cylinder gains energy from the flow when the work done is positive, and, in the opposite case, the cylinder releases energy to the flow when the work done is negative. Apparently, the transfer of energy between the cylinder and the flow predominantly occurs due to the shedding (low pass), following the total work done. The shedding-induced work done is positive when the cylinder moves from the bottom (instant (i)) to the mid ($Y = 0$) position (figure 17*c*), where C_L is induced by the growth of the shear layer on the upper side (figure 16(i,ii)). On the other hand, the work is negative when the cylinder departing from the midposition reaches the top position, where the shear layer completes its vortex shedding (figure 16(iii,iv)). The same happens when the cylinder moves from the top to the bottom (figure 17*c*). The impingement-induced work done, however, behaves differently (figure 17*b*,*d*). As the cylinder moves up from the bottom, the impingement of the vortex on the side surface (figure 16(i)) produces negative work done first (figure 17*b*,*d*). When near the trailing edge (figure 16(ii)), the impinging vortex renders positive work done, the cylinder lying close to the midposition (figure 17*d*). Its shedding (figure 16(iii,iv)) causes again negative work done (figure 17*b*,*d*) where the cylinder is away from the midposition. In other words, the work done is positive when the cylinder is around the midposition and negative when the cylinder is near the top or bottom position. Indeed, the positive work done around $Y = 0$ is useful to enhance the vibration amplitude.

Figure 18 shows the instantaneous vorticity contours for $U_r = 6$ in one vibration period. The influence of the gap vortices on the wake vortex formation is very similar to that in figure 16 for $U_r = 8$ in the LB. In each vibration period, two vortices are found to shed in the 2S mode. When the cylinder is at its bottom position, the gap

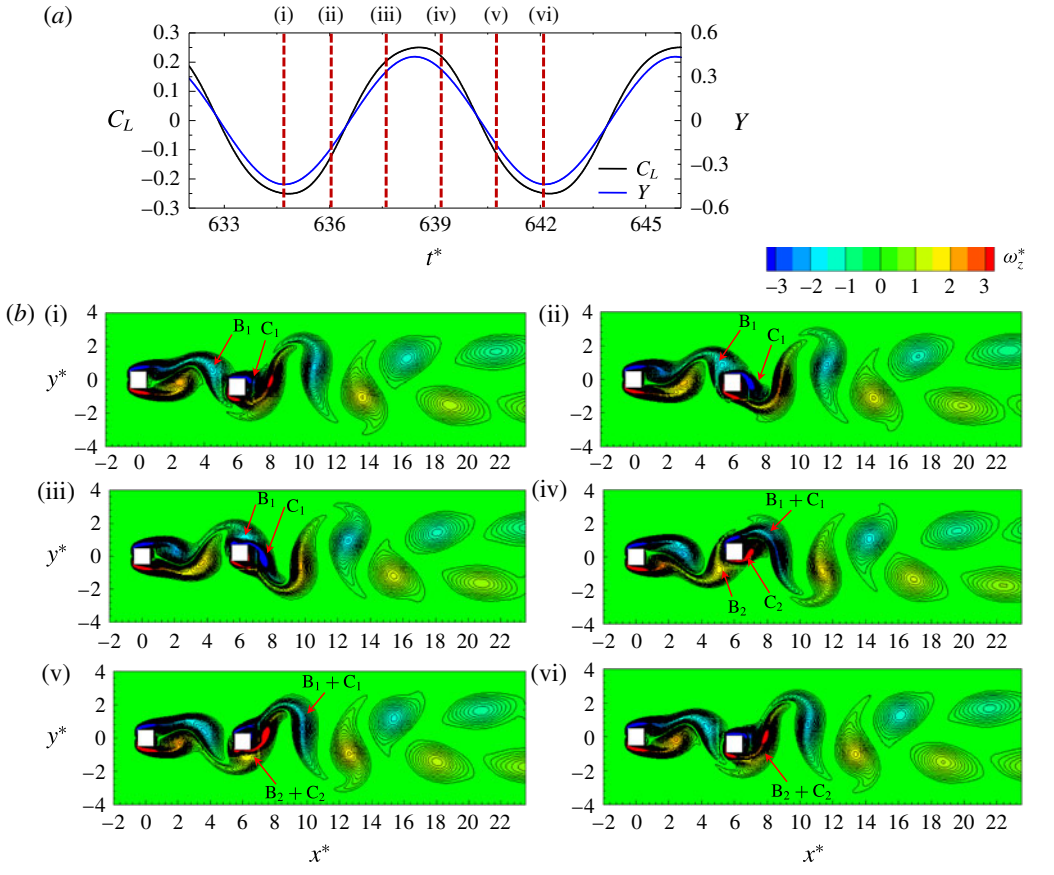

FIGURE 18. (Colour online) (*a*) Time histories of Y and C_L. (*b*) Instantaneous vorticity (ω_z^*) contours at the timings marked at the top of (*a*). Here, $U_r = 6$, $L^* = 6$ and $Re = 100$.

vortex approaches the leading edge of the cylinder (figure 18*b*(i,vi)) while it impinges on the upper surface for $U_r = 8$ (figure 16(i,vi)). Here, the low- and high-pass-filtered C_L display that the C_L induced by the shedding and impingement both are almost in phase with Y (not shown).

5.4. *Wake structure at different branches of vibration at* $Re = 200$

The dependence of the wake structure on U_r at $Re = 200$ is shown in figure 19. The wake is characterized by the 2S mode at $U_r = 1$, the C(2S) mode at $U_r = 4$, the P + S mode at $U_r = 5$–6 and the 2S mode for $U_r > 6$. The presence of the P + S mode at $U_r = 5$–6 confirms the UB. The phase of vortex shedding from the wake cylinder does not change for $U_r \leqslant 6$ (IB and UB), but changes from 0° to 180° between $U_r = 6$ (UB) and 6.5 (LB) where A^* is slashed. The wake features a 2S mode and a phase of lag 180° beyond $U_r \geqslant 6.5$ (figure 19*e*,*f*).

Figure 20 illustrates the timing and process of vortex shedding at $U_r = 6$ in one vibration period. The instants of the snapshots are marked in the time histories of C_L and Y in figure 20(*a*). Here, C_L and Y are almost in phase, indicating that the shear layers and impinging vortices contribute to the lift at the same phase. The C_L amplitude is thus enhanced, leading to a high A^* at this U_r.

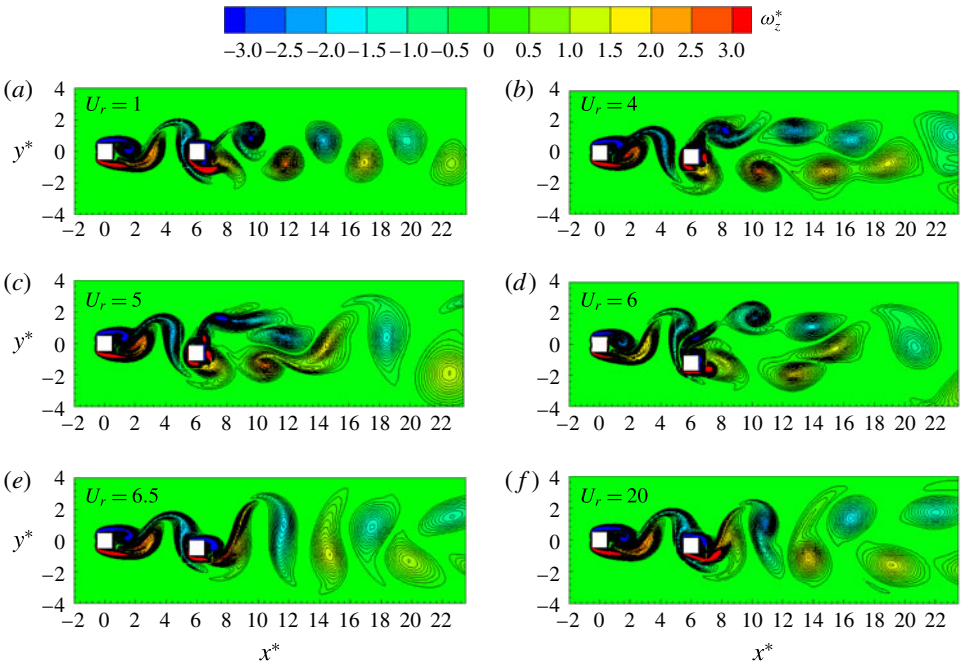

FIGURE 19. (Colour online) Instantaneous vorticity (ω_z^*) contours of upstream stationary and downstream vibrating square cylinders at various values of U_r, $L^* = 6$ and $Re = 200$.

At instant (i), the cylinder is at its top position, and vortices A–E lie around the wake cylinder. As the cylinder moves downward from instants (i)–(iv), vortex D sheds from the upper side of the cylinder and vortex E grows on the lower side, leading to a decrease in C_L (figure 20*a*). Similarly, vortex E sheds from the lower side and another vortex F grows on the upper side when the cylinder moves from the bottom to the top (instants (iv–vi)). The C_L thus increases in this half-period. In one cylinder-oscillation period, two vortices D and E shed from the two sides respectively. It is clear from figure 20(*b*) that the flow around the cylinder at instant (iv) is the mirror image of the flow at instant (i). The alternating vortex shedding thus occurs in the 2S mode, which leads to almost zero mean lift ($\bar{C}_L = -0.0022$) and zero mean displacement ($\overline{Y} = -0.0021$). However, the vortices shedding in the 2S mode arrange in a (P + S)-like mode in the wake as they evolve downstream, as marked on the snapshot at instant (vi). Since the arrangement of vortices in the (P + S)-like mode occurs downstream ($x^* > 14$), it has an insignificant impact on $\bar{C}_L$ and $\overline{Y}$.

6. Discussion

Table 3 outlines the major features of the vibration responses at different values of Re and L^*. The IB and LB appear for all of the cases, while the UB and GB materialize for the wake cylinder ($L^* = 6.0$) and single cylinder respectively, both at $Re = 200$. The DB is absent for the single cylinder at $Re = 200$. The IB, LB and DB are all delayed for the wake cylinder compared with the single cylinder. While the LB for $L^* = 2.0$ is much wider than that for the single cylinder regardless of Re, that for $L^* = 6.0$ is less wide. Both the LB and the DB are characterized by A^* decreasing with U_r. While in the literature the initial branch is known as the A^* increasing with

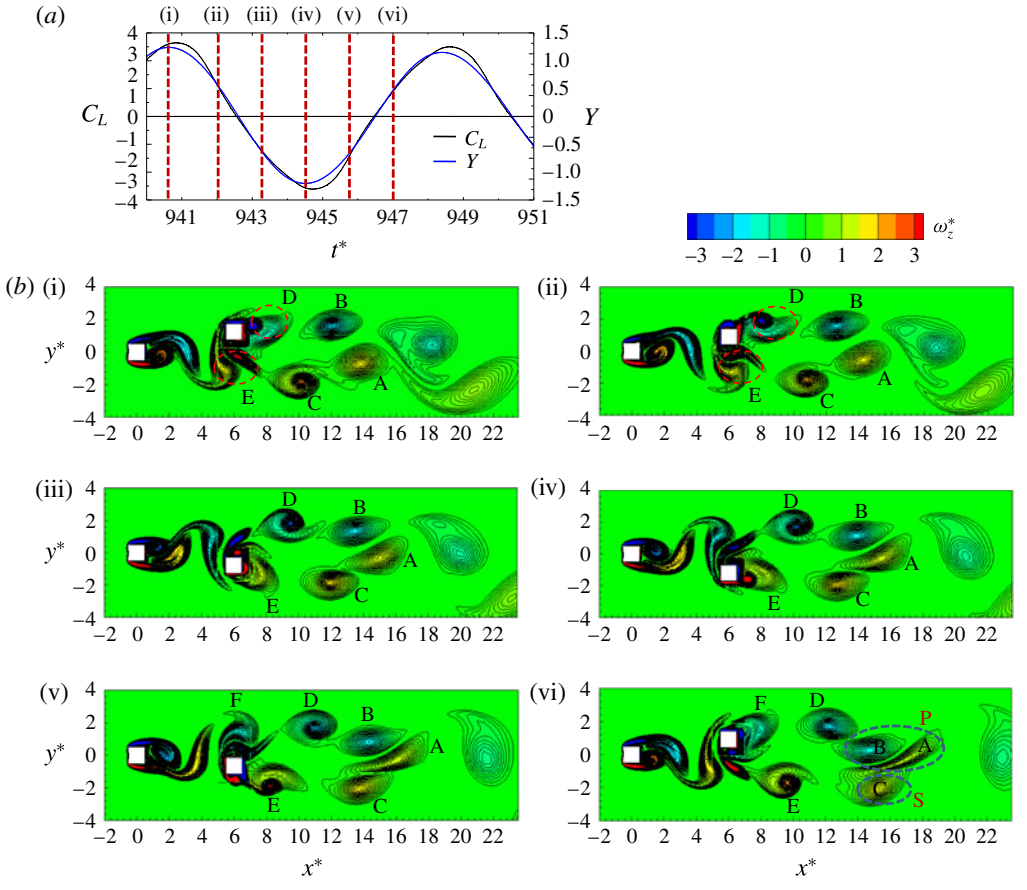

FIGURE 20. (Colour online) (*a*) Time histories of Y and C_L. (*b*) Instantaneous vorticity (ω_z^*) contours at the timings marked at the top of (*a*). Here, $U_r = 6$, $L^* = 6$ and $Re = 200$.

U_r, this is not the case for the wake cylinder at $L^* = 6.0$, $Re = 100$, where A^* first grows with U_r, followed by a decline and then another augmentation.

In the reattachment regime ($L^* = 2$), the vibration amplitude response of the wake cylinder has a similar trend to that of the single cylinder (figure 8*a*). The magnitude of A^* for the wake cylinder is, however, smaller in the IB and larger in the LB and the DB compared with its single-cylinder counterpart. The complexity of the response of the wake cylinder significantly increases at $L^* = 6$ (figure 13). Both gap-vortex impingement and wake-cylinder shedding play a role in the vibration response. Because of the impingement, the A^* of the wake cylinder is greater than that of the single cylinder for all of the regimes, except in the GB. The UB appearing for the wake cylinder at $L^* = 6$, $Re = 200$ is characterized by A^* as high as 1.2, approximately three times the maximum A^* of the single cylinder.

7. Conclusions

A numerical study at $Re = 100$ and 200 has been conducted on the flow-induced vibration of a square cylinder placed in the wake of an identical cylinder at spacing ratios of $L^* = 2$ and 6, corresponding to the reattachment and coshedding flow

https://doi.org/10.1017/jfm.2018.573 Published online by Cambridge University Press

	Cylinder	IB	UB	LB	DB	GB
$Re = 100$	Single cylinder	A^* increasing $U_r < 4.5$	—	A^* decreasing $4.5 < U_r < 10$	A^* decreasing $U_r > 10$	—
	Wake cylinder; $L^* = 2.0$	A^* increasing $U_r < 6.5$	—	A^* decreasing $6.5 < U_r < 22$	A^* decreasing $U_r > 22$	—
	Wake cylinder; $L^* = 6.0$	A^* increasing at $U_r < 5.5$, decreasing at $U_r = 5.5$–6.0 and increasing at $U_r = 6.0$–7.5	—	A^* decreasing $7.5 < U_r < 20$	A^* decreasing $U_r > 20$	—
$Re = 200$	Single cylinder	A^* increasing $U_r < 5$	—	A^* decreasing $5 < U_r \leqslant 12$	—	A^* increasing $U_r > 12$
	Wake cylinder; $L^* = 2.0$	A^* increasing $U_r < 5.5$	—	A^* decreasing $5.5 < U_r < 20$	A^* decreasing $U_r > 20$	—
	Wake cylinder; $L^* = 6.0$	A^* increasing $U_r < 5.5$	A^* increasing $5.5 < U_r < 6.5$	A^* decreasing $6.5 < U_r < 14$	A^* decreasing $U_r > 14$	—

TABLE 3. Major features of the vibration response at different values of Re and L^*.

regimes. A single cylinder was examined first to gain insight into the vibration response and corresponding flow physics. The reduced velocity U_r was varied from 1 to 30. The vibration responses, frequency responses, vortex structures and work done on the cylinder were presented and connected to the vortex shedding process. The investigation led to the following conclusions.

The single isolated cylinder experiences the IB, the LB and the DB at $Re = 100$. On the other hand, at $Re = 200$, the cylinder undergoes the IB, the LB and the GB. The vibration amplitude in the GB increases with U_r (> 12). Insight into the vibration response in the GB is imparted. At the initial stage ($12 < U_r < 24$) of the GB where the vibration amplitude rapidly grows with U_r, the galloping vibration bears combined features of the IB and the LB. The vibration amplitude is predominantly contributed by the flow features associated with the IB. On the other hand, at the late stage ($U_r > 24$) of the GB where the growth of the vibration amplitude is small, a combination of features associated with the IB and the DB prevails. Different branches can be distinguished based on the St–St_0 relationship. The IB, LB and DB follow $St < St_0$, $St > St_0$ and $St \approx St_0$ relationships respectively. In the IB, both the C_L and Y histories undergo a beat where the amplitudes of C_L and Y are not constant, but become large and small alternately. The beat results from a change in the sign of the phase lag between C_L and Y. A large amplitude corresponds to C_L leading Y, which provides positive work done on the cylinder. On the other hand, a small amplitude stems from C_L lagging Y, the cylinder releasing energy to the flow (negative work).

When the cylinder is placed in the wake of another cylinder with a separation ($L^* = 2$) corresponding to the reattachment flow regime, the IB is delayed and the LB is elongated for either Re. The vibration amplitudes in the IB and the LB are smaller and higher respectively for the wake cylinder than for the isolated cylinder. In the IB, a quasisteady reattachment of the upstream-cylinder-generated shear layers occurs on the wake cylinder, which results in a smaller amplitude for the wake cylinder than the isolated cylinder. The reattachment of the shear layers becomes alternating in the LB regime, causing the amplitude to be higher for the wake cylinder. The galloping vibration appearing for the isolated cylinder at $Re = 200$ is absent for the wake cylinder.

The vibration response of the wake cylinder at $L^* = 6$ is different from that at $L^* = 2.0$. While the IB, LB and DB are identified at $Re = 100$, an UB emerges between the IB and the LB at $Re = 200$. Again, the GB is not observed at either Re. However, the vibration amplitude is greater than that of the single cylinder for all regimes, except for the GB. The enhancement in amplitude is attributed to the interaction of the gap vortices with the wake cylinder. The vibration amplitude in the IB of the single cylinder increases with increasing U_r, which is the general characteristic of the IB, known in the literature. For the wake cylinder at $Re = 100$, the vibration amplitude in the IB first increases with increasing U_r up to $U_r = 5.5$, drastically declines between $U_r = 5.5$ and 6.0, and then increases again. This observed facet is different from that known in the literature for a single square or circular cylinder. The phase lag between the impinging vortex and the vortex shedding from the wake cylinder changes with increasing U_r, which is ascribed to such variation in the vibration amplitude. In other words, the phase lag between the impingement-induced lift and the cylinder displacement dictates the growth and decay of the vibration amplitude in the IB. The vibration amplitude becomes maximum when the impingement-induced lift is in phase with the cylinder displacement, producing the positive work done around $Y = 0$, which is useful to enhance the vibration amplitude.

Acknowledgement

Md.M.A. wishes to acknowledge the support given by the National Natural Science Foundation of China through grants 11672096 and 91752112 and by the Research Grant Council of the Shenzhen Government through grant JCYJ20170811152808282.

REFERENCES

ALAM, M. M. 2016 Lift forces induced by the phase lag between the vortex sheddings from two tandem bluff bodies. *J. Fluids Struct.* **65**, 217–237.

ALAM, M. M. & KIM, S. 2009 Free vibration of two identical circular cylinders in staggered arrangement. *Fluid Dyn. Res.* **41**, 035507.

ALAM, M. M. & MEYER, J. P. 2013 Global aerodynamic instability of twin cylinders in cross flow. *J. Fluids Struct.* **41**, 135–145.

ALAM, M. M., MORIYA, M., TAKAI, K. & SAKAMOTO, H. 2002 Suppression of fluid forces acting on two square prisms in a tandem arrangement by passive control of flow. *J. Fluids Struct.* **16** (8), 1073–1092.

ASSI, G. R. S., BEARMAN, P. W. & MENEGHINI, J. R. 2010 On the wake-induced vibration of tandem circular cylinders: the vortex interaction excitation mechanism. *J. Fluid Mech.* **661**, 365–401.

BARRERO-GIL, A., SANZ-ANDRES, A. & ROURA, M. 2009 Transverse galloping at low Reynolds numbers. *J. Fluids Struct.* **25**, 1236–1242.

BEARMAN, P. W. & OBASAJU, E. D. 1982 An experimental study of pressure fluctuations on fixed and oscillating square-section cylinders. *J. Fluid Mech.* **119**, 297–321.

BLEVINS, R. D. 1990 *Flow Induced Vibration*. Van Nostrand Reinhold.

CUI, Z., ZHAO, M., TENG, B. & CHENG, L. 2015 Two-dimensional numerical study of vortex-induced vibration and galloping of square and rectangular cylinders in steady flow. *Ocean Engng* **106**, 189–206.

DAREKAR, R. M. & SHERWIN, S. J. 2001 Flow past a square-section cylinder with a wavy stagnation face. *J. Fluid Mech.* **426**, 263–295.

DE, A. K. & DALAL, A. 2006 Numerical simulation of unconfined flow past a triangular cylinder. *Intl J. Numer. Meth. Fluids* **52**, 801–821.

GOVARDHAN, R. & WILLIAMSON, C. H. K. 2000 Modes of vortex formation and frequency response of a freely vibrating cylinder. *J. Fluid Mech.* **420**, 85–130.

HE, T., ZHOU, D. & BAO, Y. 2012 Combined interface boundary condition method for fluid–rigid body interaction. *Comput. Meth. Appl. Mech. Engng* **223–224**, 81–102.

INOUE, O., IWAKAMI, W. & HATAKEYAMA, N. 2006 Aeolian tones radiated from flow past two square cylinders in a side-by-side arrangement. *Phys. Fluids* **18**, 046104.

JAIMAN, R. K., PILLALAMARRI, N. R. & GUAN, M. Z. 2016 A stable second-order partitioned iterative scheme for freely vibrating low-mass bluff bodies in a uniform flow. *Comput. Meth. Appl. Mech. Engng* **301**, 187–215.

JOLY, A., ETIENNE, S. & PELLETIER, D. 2012 Galloping of square cylinders in cross-flow at low Reynolds numbers. *J. Fluids Struct.* **28**, 232–243.

KHALAK, A. & WILLIAMSON, C. H. K. 1999 Motions, forces and mode transitions in vortex-induced vibrations at low mass-damping. *J. Fluids Struct.* **13**, 813–851.

KIM, S., ALAM, M. M., SAKAMOTO, H. & ZHOU, Y. 2009 Flow-induced vibrations of two circular cylinders in tandem arrangement. Part 1. Characteristics of vibration. *J. Wind Engng Ind. Aerodyn.* **97**, 304–311.

KUMAR, D., SING, A. K. & SEN, S. 2018 Identification of response branches for oscillators with curved and straight contours executing VIV. *Ocean Engng* **164**, 616–627.

LUDLAM, D. V., GIL, A. B. & VELAZQUEZ, A. 2017 Flow-induced vibration of a rotating circular cylinder using position and velocity feedback. *J. Fluids Struct.* **72**, 127–151.

LUO, S. C., CHEW, Y. T. & NG, Y. T. 2003 Characteristics of square cylinder wake transition flows. *Phys. Fluids* **15** (9), 2549–2559.

MANSON, J. R., PENDER, G. & WALLIS, S. G. 1996 Limitations of traditional finite volume discretizations for unsteady computational fluid dynamics. *AIAA J.* **34** (5), 1074–1076.

MARUAI, N. M., ALI, M. S. M., ISMAIL, M. H. & ZAKI, S. A. 2018 Flow-induced vibration of square cylinder and downstream flat plate associated with micro-scale energy harvester. *J. Wind Engng Ind. Aerodyn.* **175**, 264–282.

MEHMOOD, A., ABDELKEFI, A., HAJJ, M. R., NAYFEH, A. H., AKHTAR, I. & UHAIT, A. O. 2013 Piezoelectric energy harvesting from vortex-induced vibrations of circular cylinder. *J. Sound Vib.* **332**, 4656–4667.

MITHUN, M. G. & TIWARI, S. 2014 Flow past two tandem square cylinders vibrating transversely in phase. *Fluid Dyn. Res.* **46**, 055509.

MORE, B. S., DUTTA, S., CHAUHAN, M. K. & GANDHI, B. K. 2015 Experimental investigation of flow behind two tandem square cylinders with oscillating upstream cylinder. *Exp. Therm. Fluid Sci.* **68**, 339–358.

NAKAMURA, Y. & HIRATA, K. 1991 Pressure fluctuations on oscillating rectangular cylinders with the long side normal to the flow. *J. Fluids Struct.* **5**, 165–183.

NAKAMURA, Y. & MATSUKAWA, T. 1987 Vortex excitation of rectangular cylinders with a long side normal to the flow. *J. Fluid Mech.* **180**, 171–181.

NAKAMURA, Y. & MIZOTA, T. 1975 Unsteady lifts and wakes of oscillating rectangular prisms. *ASCE J. Engng Mech.* **101**, 855–871.

NAVROSE & MITTAL, S. 2017 A new regime of multiple states in free vibration of a cylinder at low *Re*. *J. Fluids Struct.* **68**, 310–321.

PATANKAR, S. V. 1980 *Numerical Heat Transfer and Fluid Flow*. Hemisphere Publishing Corporation, Taylor and Francis Group.

QIN, B., ALAM, M. M. & ZHOU, Y. 2017 Two tandem cylinders of different diameter in cross-flow: flow-induced vibration. *J. Fluid Mech.* **829**, 621–658.

ROBICHAUX, J., BALACHANDAR, S. & VANKA, S. P. 1999 Three-dimensional Floquet instability of the wake of square cylinder. *Phys. Fluids* **11** (3), 560–578.

SAHA, A. K., BISWAS, G. & MURALIDHAR, K. 2003 Three-dimensional study of flow past a square cylinder at low Reynolds numbers. *Intl J. Heat Fluid Flow* **24**, 54–66.

SAHU, A. K., CHHABRA, R. P. & ESWARAN, V. 2009 Two-dimensional unsteady laminar flow of a power law fluid across a square cylinder. *J. Non-Newtonian Fluid Mech.* **160**, 157–167.

SAKAMOTO, H., HANIU, H. & OBATA, Y. 1987 Fluctuating forces acting on two square prisms in a tandem arrangement. *J. Wind Engng Ind. Aerodyn.* **26**, 85–103.

SEN, S. & MITTAL, S. 2011 Free vibration of a square cylinder at low Reynolds numbers. *J. Fluids Struct.* **27**, 875–884.

SEN, S. & MITTAL, S. 2015 Effect of mass ratio on free vibrations of a square cylinder at low Reynolds numbers. *J. Fluids Struct.* **54**, 661–678.

SHAABAN, M. & MOHANY, A. 2018 Flow-induced vibration of three unevenly spaced in-line cylinders in cross-flow. *J. Fluids Struct.* **76**, 367–383.

SHARMA, A. & ESWARAN, V. 2004 Heat and fluid flow across a square cylinder in the two-dimensional laminar flow regime. *Numer. Heat Transf.* **45** (3), 247–269.

SINGH, A. P., DE, A. K., CARPENTER, V. K., ESWARAN, V. & MURALIDHAR, K. 2009 Flow past a transversely oscillating square cylinder in free stream at low Reynolds numbers. *Intl J. Numer. Meth. Fluids* **61**, 658–682.

SINGH, S. & BISWAS, G. 2013 Vortex induced vibrations of a square cylinder at subcritical Reynolds numbers. *J. Fluids Struct.* **41**, 146–155.

SINGH, S. P. & MITTAL, S. 2005 Vortex-induced oscillations at low Reynolds numbers: hysteresis and vortex-shedding modes. *J. Fluids Struct.* **20**, 1085–1104.

SOHANKAR, A. 2012 A numerical investigation of the flow over a pair of identical square cylinders in a tandem arrangement. *Intl J. Numer. Meth. Fluids* **70**, 1244–1257.

SOHANKAR, A., NORBERG, C. & DAVIDSON, L. 1997 Numerical simulation of unsteady low-Reynolds number flow around rectangular cylinders at incidence. *J. Wind Engng Ind. Aerodyn.* **69–71**, 189–201.

SOHANKAR, A., NORBERG, C. & DAVIDSON, L. 1999 Simulation of three-dimensional flow around a square cylinder at moderate Reynolds numbers. *Phys. Fluids* **11** (2), 288–306.

SU, Z., LIU, Y., ZHANG, H. & ZHANG, D. 2007 Numerical simulation of vortex-induced vibration of a square cylinder. *J. Mech. Sci. Tech.* **21**, 1415–1424.

ZHAO, M. 2015 Flow-induced vibrations of square and rectangular cylinders at low Reynolds number. *Fluid Dyn. Res.* **47**, 025502.

ZHAO, M., CHENG, L. & ZHOU, T. 2013 Numerical simulation of vortex-induced vibration of a square cylinder at a low Reynolds number. *Phys. Fluids* **25**, 023603.

ZHENG, Q. & ALAM, M. M. 2017 Intrinsic features of flow past three square prisms in side-by-side arrangement. *J. Fluid Mech.* **826**, 996–1033.

ZHENG, Q. & ALAM, M. M. 2018 Fluid dynamics around three inline square prisms. *J. Fluid Mech.* (submitted).